J. Fluid Mech. (2020), *vol.* 893, A6. © The Author(s), 2020.
Published by Cambridge University Press
doi:10.1017/jfm.2020.215

Localizing effect of Langmuir circulations on small-scale turbulence in shallow water

Bing-Qing Deng[1], Zixuan Yang[1,2], Anqing Xuan[1] and Lian Shen[1,†]

[1]Department of Mechanical Engineering and St. Anthony Falls Laboratory, University of Minnesota, Minneapolis, MN 55414, USA

[2]Institute of Mechanics, Chinese Academy of Sciences, 100190 Beijing, PR China

(Received 7 July 2019; revised 27 December 2019; accepted 15 March 2020)

Wall-resolved and wall-modelled large-eddy simulations are performed to study the localizing effect of Langmuir cells (LCs) on small-scale background turbulence in shallow water. The total velocity fluctuations are decomposed into an LC content extracted by streamwise averaging and a background turbulence part. Based on the large-scale motions of LCs, the spanwise domain is divided into three regions dominated by the upwelling, spanwise and downwelling flows of LCs, respectively. The localized Reynolds stresses $\langle u_i^T u_j^T \rangle_{xt}$ in different spanwise regions are compared to show the localizing effects of the LCs on the background turbulence quantitatively, where u_1^T (or u^T), u_2^T (or v^T) and u_3^T (or w^T) represent the streamwise, vertical and spanwise components of the background turbulence velocity, respectively, and $\langle\cdot\rangle_{xt}$ denotes time and streamwise averaging. It is shown that the magnitudes of the localized Reynolds stresses in different spanwise regions vary significantly. The transport equations of the localized Reynolds stresses are then analysed to investigate the mechanisms underlying the localizing effects. It is discovered that the difference in the energy production correlated to the shear of the LC content among different regions is the key factor that leads to the localization of background turbulence. In addition, the energy production correlated to the shear of the mean flow, the energy redistribution due to the pressure–strain correlation, and the interaction between the localized Reynolds stresses and the shear of the Stokes drift also play important roles. Based on the results obtained from the analysis of the transport equations, predictive models are proposed for the localizing effects, which assess the spatial dependence of the Boussinesq model for background turbulence in coastal Langmuir turbulence. These models show good scaling performance of $\langle u^T u^T \rangle_{xt}$ near the water bottom and of $\langle -u^T v^T \rangle_{xt}$, $\langle -u^T w^T \rangle_{xt}$ and $\langle -v^T w^T \rangle_{xt}$ in the central region of the water column under various flow conditions with different values of the Reynolds number, turbulent Langmuir number and wavenumber.

Key words: turbulence simulation, wave–turbulence interactions, turbulent boundary layers

† Email address for correspondence: shen@umn.edu

1. Introduction

In oceans and lakes, interactions between surface waves and wind-driven currents can induce Langmuir cells (LCs) in the pattern of counter-rotating streamwise-elongated vortex pairs (see e.g. Langmuir 1938; Scott *et al.* 1969; Craik & Leibovich 1976; Weller & Price 1988; Smith 1992; Thorpe 1992; Farmer & Li 1995; Skyllingstad & Denbo 1995; McWilliams, Sullivan & Moeng 1997). The LCs can significantly impact the transport of mass, momentum and heat (Leibovich 1983; Smith 2001; Thorpe 2004; Sullivan & McWilliams 2010; D'Asaro 2014), and therefore influence the climate (Belcher *et al.* 2011) and ecology (Barstow 1983) in oceans and lakes. The LCs and the residual small-scale background turbulence in Langmuir turbulence constitute a multi-scale system. The investigations on LCs and their effects on background turbulence are important for the development of ocean models.

In shallow waters, LCs can engulf the entire water column and induce large-scale momentum flux (Gargett *et al.* 2004; Dethleff & Kempema 2007; Gargett & Wells 2007; Tejada-Martínez & Grosch 2007; Dierssen *et al.* 2009; Kukulka, Plueddemann & Sullivan 2012; Akan *et al.* 2013; Savidge & Gargett 2017). In the field, Gargett *et al.* (2004) and Gargett & Wells (2007) observed LCs in neutrally stratified shallow waters, and then measured the velocity fluctuations and studied the characteristics of the LCs. Based on the Craik–Leibovich (CL) equations (Craik & Leibovich 1976; Leibovich 1977), Tejada-Martínez & Grosch (2007) conducted large-eddy simulations (LES) of shallow-water Langmuir turbulence. The spanwise length scale of the LCs, the mean velocity profile and the Lumley invariant map obtained from LES (Tejada-Martínez & Grosch 2007) are in good agreement with the field measurement (Gargett & Wells 2007). In the subsequent works, experimental and LES studies were conducted to investigate shallow-water Langmuir turbulence under different environmental conditions that involve the Coriolis force (Grosch & Gargett 2016), surface heat flux (Gargett & Grosch 2014; Gargett, Savidge & Wells 2014; Walker, Tejada-Martínez & Grosch 2016), tidal currents (Kukulka *et al.* 2011; Martinat *et al.* 2011; Shrestha, Anderson & Kuehl 2018) and wave breaking (Gerbi *et al.* 2009; Li *et al.* 2013).

In neutrally stratified shallow waters, LCs impose significant impacts on turbulence statistics throughout the water column. The logarithmic layers near the water bottom and water surface are disrupted due to the vertical momentum flux induced by the LCs (Tejada-Martínez *et al.* 2012, 2013; Sinha *et al.* 2015; Deng *et al.* 2019). The LCs also alter the intensity of velocity fluctuations (Tejada-Martínez & Grosch 2007; Tejada-Martínez *et al.* 2012; Martinat, Grosch & Gatski 2014; Sinha *et al.* 2015; Deng *et al.* 2019). Owing to the contributions of the LCs, the spanwise velocity fluctuations are enhanced near the water bottom and surface, while the vertical velocity fluctuations become stronger in the central region of the water column (Tejada-Martínez & Grosch 2007; Martinat *et al.* 2014; Sinha *et al.* 2015; Deng *et al.* 2019). At high Reynolds numbers, LCs induce an additional outer peak in the profile of the streamwise Reynolds normal stress (Deng *et al.* 2019).

While LCs can induce large-scale mixing of momentum and scalars, the contribution of the background turbulence at smaller scales is also important in shallow-water Langmuir turbulence (Kukulka *et al.* 2012; Martinat *et al.* 2014; Sinha *et al.* 2015; Deng *et al.* 2019). The magnitudes of the Reynolds stresses of the background turbulence are comparable to those of the LC content in the central region of the water column and are even larger near the bottom and surface (Martinat *et al.* 2014; Sinha *et al.* 2015; Deng *et al.* 2019). As pointed out by Akan *et al.* (2013) and

Sinha *et al.* (2015), the intensity of the vertical velocity in the background turbulence is significantly enhanced near the water surface due to the Stokes drift of surface waves, and, as a result, the background turbulence is more important than LCs in the transport of mass and heat across the water surface (Gemmrich & Farmer 1999; Akan *et al.* 2013; Takagaki *et al.* 2015).

It was reported in the literature that, in other wall-bounded turbulent flows with large-scale structures, the intensity of the residual background turbulence is significantly modulated by the large-scale structures (Hutchins & Marusic 2007; Mathis, Hutchins & Marusic 2009; Anderson 2016; Dai, Huang & Xu 2016; Deng, Huang & Xu 2016; Salesky & Anderson 2018). Specifically, in the high-Reynolds-number turbulent boundary layer, the near-wall background turbulence is locally enhanced and suppressed in the regions with high-speed and low-speed large-scale motions, respectively (Hutchins & Marusic 2007; Mathis *et al.* 2009). This finding inspired the development of new turbulence models. For example, new wall-layer models were developed to account for the localizing effect of large-scale structures on the background turbulence, which improved the performance of LES in predicting near-wall turbulence statistics (Inoue *et al.* 2012; Howland & Yang 2018; Yin, Huang & Xu 2018).

Compared with the large-scale structures in turbulent boundary layers, LCs are more organized and energetic (Tejada-Martínez & Grosch 2007; Deng *et al.* 2019), and therefore are expected to impose a more significant localizing effect on the background turbulence. In the investigation of scalar transport near the sea surface, Akan *et al.* (2013) observed that streaks consisting of large-magnitude streamwise velocity of background turbulence are concentrated above the downwelling limbs of LCs, where the streamwise velocity of the LC content is positive. Takagaki *et al.* (2015) noted that the small-scale vortices are intensified in the surface convergent regions with positive streamwise velocity of the LC content. The findings of Akan *et al.* (2013) and Takagaki *et al.* (2015) explain the observation in the field that small windrows occur at the two flanks of the main windrows to form a 'Y'-junction pattern (Langmuir 1938; Scott *et al.* 1969; Assaf, Gerard & Gordon 1971; Weller & Price 1988; Thorpe 1992; Farmer & Li 1995). Martinat *et al.* (2014) observed that the statistics of background turbulence averaged over time and the horizontal plane are different from those without applying the spanwise averaging. This observation indicates that the intensities of background turbulence vary with the spanwise location. Martinat *et al.* (2014) further stressed that the localizing effect of LCs on the background turbulence needs to be considered in the Reynolds-averaged Navier–Stokes (RANS) simulation of Langmuir turbulence.

To date, the localizing effect of the LCs on the background turbulence has not been studied systematically. The following questions associated with the localizing effect need to be answered:

(1) Is the localizing effect of the LCs on the background turbulence in the bottom boundary layer similar to that in the surface boundary layer?
(2) What is the underlying mechanism for the localizing effect?
(3) How does one develop models that predict the localized turbulence intensity or momentum flux of the background turbulence?

To answer the above questions, in this study we further analyse the LES database of shallow-water Langmuir turbulence obtained by Deng *et al.* (2019). The LCs and background turbulence are quantified based on a triple decomposition of the flow field, and the localized Reynolds stresses are defined as the time and streamwise average of

the second moments of the background turbulence velocity fluctuations. A comparison of the localized Reynolds stresses at different spanwise locations shows the localizing effects quantitatively. The transport equations of the localized Reynolds stresses are derived, and the dominant sources in the budget balance of the localized Reynolds stresses are analysed to reveal the mechanisms underlying the localizing effect, based on which predictive models are proposed to scale the localized Reynolds stresses.

The remainder of this paper is organized as follows. The simulation method and computational cases are introduced in § 2. In § 3, how the intensities of the background turbulence vary in the spanwise direction is revealed. In § 4, the key mechanisms underlying the localizing effect are studied through the analyses of the budget terms in the transport equations of the localized Reynolds stresses. In § 5, predictive models of the localized Reynolds stresses are proposed based on the key mechanisms found in § 4 to assess the spatial dependence of Boussinesq-model parameters in shallow-water Langmuir turbulence for the localized Reynolds stresses. The localizing effects at a practical Reynolds number are further discussed in § 6. Finally, our main conclusions are given in § 7.

2. Simulation method and computational cases

2.1. *Governing equations*

The localizing effects of LCs on the background turbulence are mainly studied through the analyses of the database obtained from the wall-resolved LES (Deng *et al.* 2019) and wall-modelled LES of neutrally stratified shallow-water Langmuir turbulence. The following continuity and CL equations (McWilliams *et al.* 1997; Tejada-Martínez & Grosch 2007) were simulated:

$$\frac{\partial \overline{u}_i}{\partial x_i} = 0, \tag{2.1}$$

$$\frac{\partial \overline{u}_i}{\partial t} + \overline{u}_j \frac{\partial \overline{u}_i}{\partial x_j} = -\frac{1}{\rho}\frac{\partial \overline{\Pi}}{\partial x_i} + \nu \frac{\partial^2 \overline{u}_i}{\partial {x_j}^2} + \epsilon_{ijk} u_j^S \overline{\omega}_k + \frac{\partial \tau_{ij}^{sgs}}{\partial x_j}. \tag{2.2}$$

The coordinates x_1, x_2 and x_3 (or x, y and z) denote the streamwise, vertical and spanwise directions, respectively, with $\overline{u}_1$, $\overline{u}_2$ and $\overline{u}_3$ (or $\overline{u}$, $\overline{v}$ and $\overline{w}$) representing the corresponding velocity components. The overline stands for the implicit grid-level filter in LES. The effective pressure $\overline{\Pi}$ is the summation of the resolved pressure $\overline{p}$ and an additional part $\overline{\Gamma}$ defined as (McWilliams *et al.* 1997)

$$\overline{\Gamma} = 0.5 u_j^S u_j^S + u_j^S \overline{u}_j. \tag{2.3}$$

The third term on the right-hand side of (2.2) is the CL vortex forcing term, where ϵ_{ijk} is the third-order Levi-Civita symbol, $\overline{\omega}_i = \epsilon_{ijk}\partial \overline{u}_k/\partial x_j$ is the resolved vorticity and u_i^S is the Stokes drift velocity induced by the water wave. In shallow water, u_i^S is given as (Tejada-Martínez & Grosch 2007)

$$u_1^S = u^{S*}\frac{\cosh(2ky)}{2\sinh^2(2kh)} = \frac{u_\tau}{La_t^2}\frac{\cosh(2ky)}{2\sinh^2(2kh)}, \quad u_2^S = u_3^S = 0, \quad y \in [0, 2h]. \tag{2.4a,b}$$

Here, u^{S*} is the characteristic velocity of the Stokes drift of water waves in shallow water (Tejada-Martínez & Grosch 2007), which is defined as $u^{S*} = \sigma k a^2$, with σ, k and a being the frequency, wavenumber and wave amplitude, respectively. The water

Case	Re_τ	La_t	kh	L_x/h	L_z/h	N_x	N_y	N_z	Δx^+	Δy^+_{min}	Δz^+
1	1000	0.7	0.5	8π	$16\pi/3$	512	192	512	49.09	0.625	32.72
2	700	0.7	0.5	8π	$16\pi/3$	384	144	384	45.81	0.588	30.54
3	395	0.7	0.5	8π	$16\pi/3$	256	128	256	38.78	0.395	25.85
4	1000	0.7	1.0	8π	$16\pi/3$	512	192	512	49.09	0.625	32.72
5	1000	0.9	0.5	8π	$16\pi/3$	512	192	512	49.09	0.625	32.72
6	1000	∞	—	8π	$16\pi/3$	512	192	512	49.09	0.625	32.72
7	395	0.7	0.5	32π	$64\pi/3$	1024	128	1024	38.78	0.395	25.85
8	10 000	0.7	0.5	8π	$16\pi/3$	256	192	256	981.75	52	645.5

TABLE 1. Key parameters of simulation cases.

depth is $2h$. The surface friction velocity u_τ equals $\sqrt{\tau_w/\rho}$, where τ_w is the wind stress imposed on the surface and ρ is the density of water. The turbulent Langmuir number $La_t = \sqrt{u_\tau/u^{S*}}$ characterizes the relative importance of the wind shear to the CL vortex force related to the Stokes drift of surface waves (McWilliams *et al.* 1997). From (2.2) and (2.4), it is understood that the magnitude of the CL vortex force decreases monotonically as the value of either La_t or kh increases. In the last term of (2.2), τ_{ij}^{sgs} is the subgrid-scale (SGS) stress tensor, calculated using the dynamic Smagorinsky model (Smargorinsky 1963; Germano *et al.* 1991; Lilly 1992).

Periodic boundary conditions are applied in the streamwise (x) and spanwise (z) directions. At the water bottom ($y = 0$), the no-slip boundary condition is imposed. In wall-resolved LES, the bottom boundary condition is $u = v = w = 0$. In wall-modelled LES, the vertical velocity at the bottom is zero, and the streamwise and spanwise shear stresses at the bottom are calculated using the equilibrium-stress model (Balaras, Benocci & Piomelli 1995; Pope 2001; Piomelli & Balaras 2002)

$$\frac{\tau_{i2}(x, z, t)}{\rho} = \left[\frac{\kappa U(x, y, z, t)}{\log(y/y_0)}\right]^2 \frac{\overline{u}_i(x, y, z, t)}{U(x, y, z, t)}, \quad i = 1, 3. \tag{2.5}$$

In this model, $U(x, y, z, t)$ is the magnitude of the horizonal component of the velocity. The von Kármán constant κ is set to 0.37 following the law of the wall found in our previous wall-resolved LES study (Deng *et al.* 2019). The bottom roughness y_0/h is set to be 0.02 (Shrestha, Tejada-Martinez & Kuehl 2019). Following the literature (Craik & Leibovich 1976; Leibovich 1977; Skyllingstad & Denbo 1995; McWilliams *et al.* 1997; Tejada-Martínez & Grosch 2007), the rigid-lid condition with a constant wind shear stress τ_w is prescribed at the top of the computational domain ($y = 2h$), which are $\tau_{12} = \tau_w$, $v = 0$ and $\tau_{32} = 0$ at $y = 2h$ for both the wall-resolved and wall-modelled LES. The equations are solved using a hybrid second-order finite difference and pseudo-spectral method (Kim & Moin 1985). The second-order Adams–Bashforth method is used for time integration. More details of the numerical method and its validation are given in Deng *et al.* (2019).

2.2. *Simulation cases*

Table 1 summarizes the key parameters of the simulation cases used to study the localizing effect of LCs on background turbulence, including the Reynolds number $Re_\tau = u_\tau h/\nu$, with ν being the kinematic viscosity, dimensionless wavenumber kh, turbulent Langmuir number La_t, computational domain size $L_x \times L_y \times L_z$, number of

grid points $N_x \times N_y \times N_z$, and grid resolution Δx^+, Δy^+_{min} and Δz^+. In this paper, the superscript '+' is used to denote non-dimensional quantities normalized using wall units ν/u_τ and the friction velocity u_τ as the characteristic length and velocity scales, respectively. The computational domain size is set to $8\pi h \times 2h \times 16\pi h/3$ in cases 1–6. To ensure that this computational domain size is sufficiently large to capture the localizing effects of LCs on the background turbulence, we conducted another simulation with a larger computational domain size of $32\pi h \times 2h \times 64\pi h/3$, denoted as case 7 in table 1. The other parameters of case 7 are the same as those of case 3. It is shown in the Appendix that the results of cases 3 and 7 are consistent, indicating that the computational domain size for cases 1–6 is sufficient. In the wall-resolved LES cases (cases 1–7), the grid is refined near the bottom and top of the computational domain, and Δy^+_{min} is the resolution of the first grid near the top or bottom. The grid resolution used in cases 1–7 (table 1) meets the requirement of wall-resolved LES (Chapman 1979; Choi & Moin 2012). In the wall-modelled LES case (case 8), the vertical grid is evenly distributed, and the first point is located in the logarithmic layer (Deng *et al.* 2019).

In case 1 (table 1), the values of kh and La_t are given consistent with the observations in the field (Gargett & Wells 2007), and as such this case is used to start the analyses of the localizing effects of LCs on the background turbulence. Other cases are then used to examine the localizing effect of LCs at various Re_τ, La_t and kh shown in §§ 5 and 6. From case 1 to case 3, the Reynolds number changes from 1000 to 395 to study the influence of the Reynolds number, while the values of La_t and kh remain unchanged. Case 8 is conducted to study the localizing effects of LCs on background turbulence at a practical Reynolds numbers $Re_\tau = 10^4$. To investigate the effect of the wavenumber kh, its value is set to 0.5 and 1.0 in cases 1 and 4, respectively. The effect of La_t is studied by comparing the results of cases 1 and 5, in which the values of La_t are set to 0.7 and 0.9, respectively. Case 6 without the vortex forcing is used as a reference case for the velocity scaling study in § 5.

2.3. *Definition of turbulence statistics*

To analyse the localizing effect of LCs on the background turbulence, the velocity is decomposed into the mean velocity $\langle u_i \rangle$, the LC content velocity u_i^L and the background turbulence velocity fluctuations u_i^T as

$$u_i(x, y, z, t) = \langle u_i \rangle(y) + u_i'(x, y, z, t) = \langle u_i \rangle(y) + u_i^L(y, z, t) + u_i^T(x, y, z, t). \tag{2.6}$$

Because all the quantities studied in this paper are implicitly filtered at the grid level, the overline is omitted to simplify the presentations hereinafter. A pair of angular brackets $\langle \cdot \rangle$ is used to denote the time and plane averaging, *viz.*

$$\langle u_i \rangle(y) = \frac{1}{L_x L_z (T_2 - T_1)} \int_{T_1}^{T_2} \int_0^{L_z} \int_0^{L_x} u_i(x, y, z, t)\, \mathrm{d}x\, \mathrm{d}z\, \mathrm{d}t. \tag{2.7}$$

Here, T_1 and T_2 indicate the starting and ending instants of the time interval, respectively. The total velocity fluctuation u_i' is defined as the difference between u_i and $\langle u_i \rangle$. Because the LCs are elongated in the streamwise direction, the LC content velocity u_i^L is extracted using the streamwise averaging as

$$u_i^L(y, z, t) = \langle u_i' \rangle_x(y, z, t) = \frac{1}{L_x} \int_0^{L_x} u_i'(x, y, z, t)\, \mathrm{d}x, \tag{2.8}$$

where $\langle\cdot\rangle_x$ stands for the averaging in the streamwise direction x. The background turbulence velocity u_i^T is then defined as

$$u_i^T(x, y, z, t) = u_i'(x, y, z, t) - u_i^L(y, z, t). \tag{2.9}$$

The present triple decomposition given by (2.6) has the same spirit as but different form from the one proposed by Reynolds & Hussain (1972), in which the velocity field is decomposed into the time-averaged mean flow, the organized wave motion and the turbulent motion based on the characteristic temporal frequency of the components. In contrast, the present triple decomposition is based on the characteristic spatial length scale of different components. The triple decomposition used in the present study is similar to that introduced by Papavassiliou & Hanratty (1997) in their investigation of Couette cells in turbulent Couette flows and later applied by Tejada-Martínez & Grosch (2007) in their analysis of LCs in shallow-water Langmuir turbulence. According to Tejada-Martínez & Grosch (2007), the present triple decomposition based on the spatial length scale is effective in capturing the LCs.

From the definition of velocity fluctuations, it is known that

$$\langle u_i'\rangle = \langle u_i'\rangle_{xzt} = 0. \tag{2.10}$$

Substituting the definition of u_i^L given by (2.8) into (2.10), it is found that

$$\langle u_i^L\rangle_{zt} = 0. \tag{2.11}$$

However, because u_i^L is inhomogeneous in the spanwise direction (figure 1) but homogeneous in time, the spanwise averaging is not equivalent to time averaging. As a result, the time averaging of u_i^L is not zero, i.e.

$$\langle u_i^L\rangle_t \neq 0. \tag{2.12}$$

A non-zero time-averaged u_i^L was also found when the Couette cells (Papavassiliou & Hanratty 1997) or full-depth LCs (Tejada-Martínez & Grosch 2007) exist.

Figures 1(*a*) and 1(*b*) show the instantaneous flow fields of u_i^L in a y–z plane at times $tu_\tau/h = 175$ and 295, respectively. It can be observed that LCs appear in the pattern of counter-rotating vortex pairs, accompanied by positive and negative LC content streamwise velocity (u^L) in the downwelling and upwelling limbs, respectively. The pattern of contours and vectors shown in figure 1(*a*,*b*) is consistent with the results of Tejada-Martínez & Grosch (2007). By contrasting figure 1(*a*) with figure 1(*b*), it is evident that the LC content velocity fields at two different instants are similar, indicating that the spanwise location of the LCs remains almost unchanged during the simulation. This observation can further be confirmed using the time history of the LC content velocity. Figure 1(*c*) displays the contours of u^L in a z–t plane at the vertical location $y/h = 0.1$. It is shown that the contours of u^L are nearly stationary in time, indicating that the spanwise location of the LCs is approximately fixed. In field measurements in coastal regions, the full-depth LCs are transient mainly due to their spanwise movement induced by the spanwise tidal motion (Gargett & Wells 2007). However, the characteristic time scale of the background turbulence is much shorter than that of LCs, such that the LCs can be regarded as persistent structures in the analyses of the localization effect of LCs on the background turbulence. It has also been demonstrated that most of the statistics

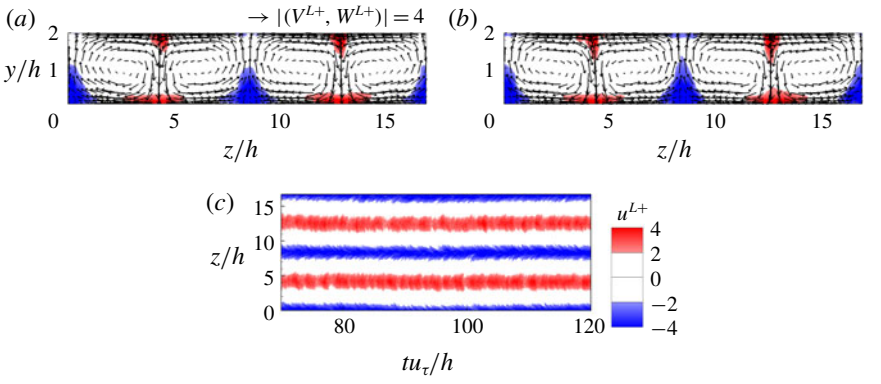

FIGURE 1. Spatial and temporal variation of the LC content velocity u_i^L. (*a*,*b*) Instantaneous fields of u_i^L in a cross-stream plane at $tu_\tau/h = 175$ and 295, respectively. The contours show the streamwise component u^{L+}, while the vectors consist of (v^{L+}, w^{L+}). (*c*) Contours of u^{L+} in a z–t plane at $y/h = 0.1$. The results of case 1 are shown.

obtained from the LES of Tejada-Martínez & Grosch (2007) in the absence of the spanwise tidal motion agree with those obtained from the field measurement of Gargett & Wells (2007).

Because the spanwise locations of streamwise-elongated LCs remain stable over time, the LC content velocities significantly vary only with the vertical and spanwise coordinates in the y–z plane. The localizing effect of LCs on the background turbulence can be revealed by comparing the distribution of the intensities of background turbulence in the y–z plane with that of the LC content velocity. Therefore, time and streamwise averaging is used to define the localized Reynolds stresses as

$$\langle u_i^T u_j^T \rangle_{xt}(y, z) = \frac{1}{L_x(T_2 - T_1)} \int_{T_1}^{T_2} \int_0^{L_x} u_i^T(x, y, z, t) u_j^T(x, y, z, t)\, \mathrm{d}x\, \mathrm{d}t, \tag{2.13}$$

where $\langle\cdot\rangle_{xt}$ denotes the time and streamwise averaging. The time-averaged statistics shown herein are obtained using over 1200 instantaneous snapshots, corresponding to a time duration of $T_2 - T_1 = 120h/u_\tau$. To examine if the number of snapshots is sufficient, we compared the results based on 1200 and 600 snapshots. It was observed that reducing the number of snapshots by half results in a change in $\langle u_i^T v_j^T \rangle_{xt}$ by less than 1.2 %.

Based on the time-averaged vertical component of the LC content velocity, $\langle v^L \rangle_t$, the spanwise location can be divided into the downwelling-motion region (D-region), upwelling-motion region (U-region) and horizontal-motion region (H-region) as shown schematically in figure 2, which displays the contours of $\langle u^L \rangle_t$ and isopleths of $\langle v^L \rangle_t = \pm 0.3 \max(\langle v^L \rangle_t)$. Hereinafter, $\langle\cdot\rangle_t$ represents averaging in time. The streamlines are superimposed to show the location of the LCs. The three regions are separated by dash-dotted lines, defined as the vertical tangent lines of the isopleths of $\langle v^L \rangle_t = \pm 0.3 \max(|\langle v^L \rangle_t|)$. In the D-region and U-region, the vertical motions of LCs are strong, characterized by large negative and positive values of $\langle v^L \rangle_t$, respectively. In the H-region, the spanwise motion of LCs is dominant, while the magnitude of $\langle v^L \rangle_t$ is relatively small.

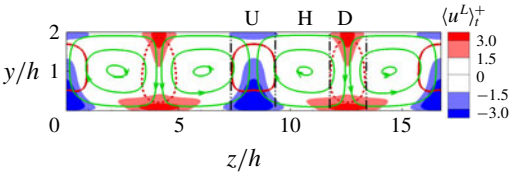

FIGURE 2. Time-averaged LC content velocity field $\langle u_i^L\rangle_t^+$. The contours show the value of $\langle u^L\rangle_t^+$, the solid and dashed black lines represent the isopleth of $\langle v^L\rangle_t^+ = 0.3\max(\langle v^L\rangle_t)$ and $-0.3\max(\langle v^L\rangle_t)$, respectively, and the solid green lines with arrows are the streamlines of LCs on the vertical y–z plane. The dash-dotted black vertical lines divide the spanwise locations into the U-, H- and D-regions, which are dominated by the upwelling, spanwise and downwelling motions of the LCs, respectively. The results of case 1 are shown.

3. Localizing effect of LCs on background turbulence

In this section, the localizing effect of LCs on the background turbulence is studied using case 1 as a representative case. Other cases are used to examine the localizing effect at various parameters in § 5. The localizing effects of LCs on the background turbulence can be studied quantitatively using the localized Reynolds stresses $\langle u_i^T u_j^T\rangle_{xt}$. Let DC, HC and UC denote the spanwise centres of the D-region, H-region and U-region, respectively. Figure 3 compares the vertical profiles of $\langle u_i^T u_j^T\rangle_{xt}$ near the water bottom ($y/h \leqslant 0.1$) at DC, HC and UC. Figure 3(a) shows that, below $y/h = 0.04$, the magnitude of $\langle u^T u^T\rangle_{xt}$ is larger at DC than at HC and UC. It is striking that the peak value of $\langle u^T u^T\rangle_{xt}$ at DC is approximately three times that at UC. Although a localizing effect of large-scale motions on small-scale streamwise velocity was also observed in wall-bounded turbulence without LCs (Mathis *et al.* 2009; Inoue *et al.* 2012), the localizing effect of LCs on u^T is much more significant in the shallow-water Langmuir turbulence studied here. For example, in turbulent channel flows, the magnitude ratio between $\langle u^T u^T\rangle_{xt}$ collocating with positive and negative large-scale streamwise velocity is only 1.2 (Jimenez 2012; Deng *et al.* 2016), while this ratio is approximately 3.0 in the shallow-water Langmuir turbulence. As the distance from the bottom increases from $y/h = 0.015$ to 0.1, the value of $\langle u^T u^T\rangle_{xt}$ decreases faster at DC than at UC and HC. Consequently, the magnitude of $\langle u^T u^T\rangle_{xt}$ at DC becomes smaller than that at HC and UC above $y/h = 0.04$ and 0.07, respectively. From figure 3(b), it is seen that the magnitude of $\langle v^T v^T\rangle_{xt}$ is smaller at UC than at both HC and DC below $y/h = 0.1$. Below $y/h = 0.02$, the magnitudes of $\langle v^T v^T\rangle_{xt}$ at HC and DC are comparable, while above $y/h = 0.02$, the intensity of v^T is stronger at HC than at DC. Figure 3(c) shows that the magnitudes of $\langle w^T w^T\rangle_{xt}$ at DC and UC are, respectively, the largest and smallest among the three spanwise locations.

The above results of the localized Reynolds normal stresses reveal the localizing effect of LCs on the intensity of the background turbulence. Correspondingly, the momentum flux of the background turbulence is also localized by the LCs. As shown in figure 3(d), below $y/h = 0.03$, the magnitudes of the localized Reynolds shear stress $\langle -u^T v^T\rangle_{xt}$ at DC and UC are, respectively, larger and smaller than that at HC, indicating the enhancement and suppression of momentum flux in the D- and U-regions, respectively. As the distance from the bottom increases to $y/h \geqslant 0.03$ and $y/h \geqslant 0.07$, the magnitude of $\langle -u^T v^T\rangle$ at DC becomes smaller than that at HC and UC, respectively. Such a change in the localizing effect of LCs on $\langle -u^T v^T\rangle$ is similar to that on $\langle u^T u^T\rangle$.

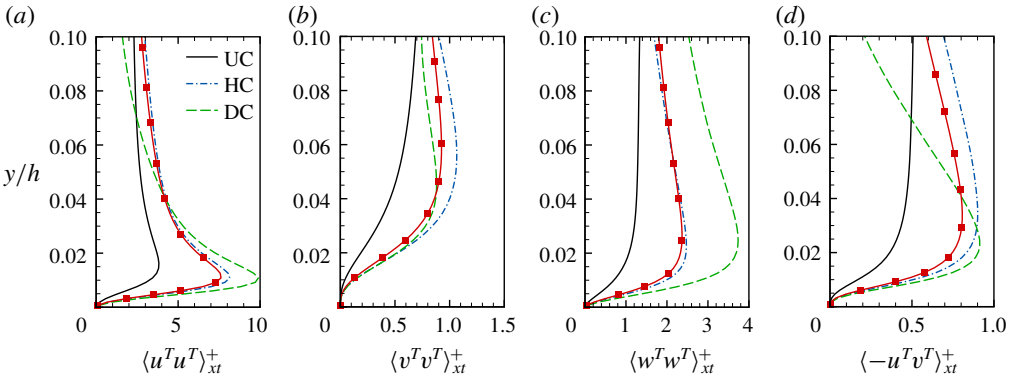

FIGURE 3. Vertical profiles of localized Reynolds stresses $\langle u_i^T u_j^T \rangle_{xt}$ at UC, HC and DC near the water bottom: (*a*) $\langle u^T u^T \rangle_{xt}$, (*b*) $\langle v^T v^T \rangle_{xt}$, (*c*) $\langle w^T w^T \rangle_{xt}$ and (*d*) $\langle -u^T v^T \rangle_{xt}$. The lines with squares represent the Reynolds stresses $\langle u_i^T u_j^T \rangle$ based on the time and plane averaging. The results of case 1 are shown.

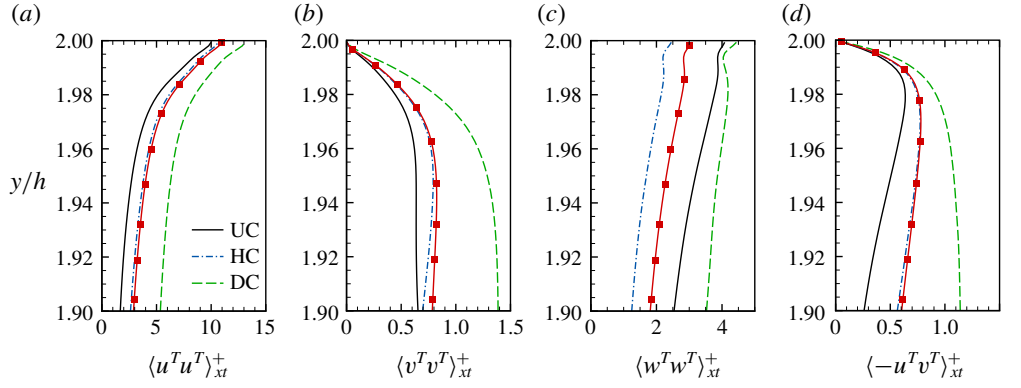

FIGURE 4. Vertical profiles of localized Reynolds stresses $\langle u_i^T u_j^T \rangle_{xt}$ at UC, HC and DC near the surface: (*a*) $\langle u^T u^T \rangle_{xt}$, (*b*) $\langle v^T v^T \rangle_{xt}$, (*c*) $\langle w^T w^T \rangle_{xt}$ and (*d*) $\langle -u^T v^T \rangle_{xt}$. The lines with squares represent the Reynolds stresses $\langle u_i^T u_j^T \rangle$ based on the time and plane averaging. The results of case 1 are shown.

To explore the localizing effect of LCs on the background turbulence in the near-surface region, the vertical profiles of $\langle u_i^T u_j^T \rangle_{xt}$ for $y/h \geqslant 1.9$ at DC, HC and UC are compared in figure 4. The localizing effects of LCs on $\langle u^T u^T \rangle_{xt}$, $\langle v^T v^T \rangle_{xt}$ and $\langle -u^T v^T \rangle_{xt}$ are similar near the surface. As shown in figure 4(*a*,*b*,*d*), their magnitudes are, respectively, smaller and larger at UC and DC than at HC. The localizing effect on $\langle w^T w^T \rangle_{xt}$ is different from the other three components in the near-surface region. The magnitude of $\langle w^T w^T \rangle_{xt}$ is larger at UC and DC than at HC (figure 4*c*). The localizing effects of LCs on the background turbulence shown above statistically can also be observed from the instantaneous fields of u_i^T at $y/h = 0.015$ and 1.985 in §A of the supplementary material (available at https://doi.org/10.1017/jfm.2020.215).

The LCs also influence the background turbulence in the central region of the water column. Figure 5 shows the contours of $\langle u_i^T u_j^T \rangle_{xt}$ in the y–z plane. It is observed from figure 5(*a–f*) that, except for $\langle -v^T w^T \rangle_{xt}^+$, the effects of LCs on the other five

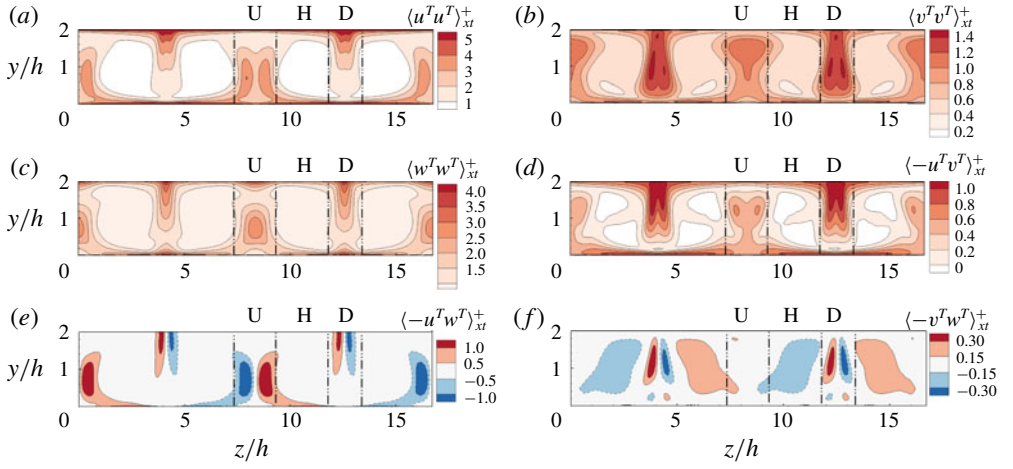

FIGURE 5. Contours of localized Reynolds stresses $\langle u_i^T u_j^T\rangle_{xt}$ on the vertical y–z plane: (*a*) $\langle u^T u^T\rangle_{xt}$, (*b*) $\langle v^T v^T\rangle_{xt}$, (*c*) $\langle w^T w^T\rangle_{xt}$, (*d*) $\langle -u^T v^T\rangle_{xt}$, (*e*) $\langle -u^T w^T\rangle_{xt}$ and (*f*) $\langle -v^T w^T\rangle_{xt}$. The results of case 1 are shown.

components of $\langle u_i^T u_j^T\rangle^+_{xt}$ are similar in the central region of the water column. There are two regions where the magnitudes of $\langle u_i^T u_j^T\rangle$ are enhanced. These two regions are located in the U-region and D-region, connecting with the water bottom and water surface, respectively. The strong large-scale vertical motions of LCs in the U- and D-regions promote the vertical transport of scalar and momentum throughout the water column (Kukulka & Harcourt 2017). Moreover, the locally strong v^T and $\langle -u^T v^T\rangle_{xt}$ in the U- and D-regions also enhance the vertical transport in the central region of the water column. On the other hand, while the large-scale spanwise motions of LCs are weak in the central region, the strong w^T and $\langle -u^T w^T\rangle_{xt}$ can induce scalar and momentum transport along the spanwise direction in the D- and U-regions. Compared with other components of $\langle u_i^T u_j^T\rangle^+_{xt}$, the localizing effects of LCs on $\langle -v^T w^T\rangle$ are different. As shown in figure 5(*f*), $\langle -v^T w^T\rangle^+_{xt}$ is suppressed in the U-region and enhanced in the D-region. Furthermore, $\langle -v^T w^T\rangle^+_{xt}$ is smaller in magnitude than other components of $\langle u_i^T u_j^T\rangle_{xt}$, indicating that $\langle -v^T w^T\rangle^+_{xt}$ does not play an important role in the shallow-water Langmuir turbulence. A comparison of the spanwise variation of $\langle u_i^T u_j^T\rangle_{xt}$ near the bottom, in the central region and near the surface indicates that the localizing effects of LCs are different in these three regions, which is further explained by analysing the transport equations of $\langle u_i^T u_j^T\rangle_{xt}$ in § 4.

4. Budget of localized Reynolds stresses

4.1. *Transport equations of localized Reynolds stresses*

In this section, the mechanism underlying the localizing effect of LCs on background turbulence is studied through the analyses of the budget terms in the transport equations of the localized Reynolds stresses, which can be written as

$$\frac{\partial\langle u_i^T u_j^T\rangle_{xt}}{\partial t} + (\langle u_k\rangle + u_k^S)\frac{\partial\langle u_i^T u_j^T\rangle_{xt}}{\partial x_k} = P_{ij}^M + \Pi_{ij} + D_{ij} + T_{ij} + V_{ij} + \varepsilon_{ij} + S_{ij} + P_{ij}^L + T_{ij}^L. \tag{4.1}$$

The budget terms on the right-hand side of the above equation are the mean-shear production term P_{ij}^M, pressure diffusion term Π_{ij}, pressure–strain correlation term D_{ij}, background turbulence diffusion term T_{ij}, viscous diffusion term V_{ij}, dissipation term ε_{ij}, Stokes forcing term S_{ij}, LC content production term P_{ij}^L and LC content turbulence diffusion term T_{ij}^L, respectively. These are defined as follows:

$$P_{ij}^M = -\langle u_j^T u_k^T \rangle_{xt} \frac{\partial \langle u_i \rangle}{\partial x_k} - \langle u_i^T u_k^T \rangle_{xt} \frac{\partial \langle u_j \rangle}{\partial x_k}, \tag{4.2}$$

$$\Pi_{ij} = -\frac{\partial \langle p^T u_j^T \rangle_{xt}}{\partial x_i} - \frac{\partial \langle p^T u_i^T \rangle_{xt}}{\partial x_j}, \tag{4.3}$$

$$D_{ij} = \left\langle p^T \left(\frac{\partial u_j^T}{\partial x_i} + \frac{\partial u_i^T}{\partial x_j} \right) \right\rangle_{xt}, \tag{4.4}$$

$$T_{ij} = -\frac{\partial \langle u_i^T u_j^T u_k^T \rangle_{xt}}{\partial x_k}, \tag{4.5}$$

$$V_{ij} = \frac{\partial}{\partial x_k} \left\langle \nu \frac{\partial u_i^T u_j^T}{\partial x_k} + u_j^T (\tau_{ik}^{sgs})^T + u_i^T (\tau_{jk}^{sgs})^T \right\rangle_{xt}, \tag{4.6}$$

$$\varepsilon_{ij} = -\left\langle 2\nu \frac{\partial u_i^T}{\partial x_k} \frac{\partial u_j^T}{\partial x_k} + (\tau_{ik}^{sgs})^T \frac{\partial u_j^T}{\partial x_k} + (\tau_{jk}^{sgs})^T \frac{\partial u_i^T}{\partial x_k} \right\rangle_{xt}, \tag{4.7}$$

$$S_{ij} = -\langle u_i^T u_k^T \rangle_{xt} \frac{\partial u_k^S}{\partial x_j} - \langle u_j^T u_k^T \rangle_{xt} \frac{\partial u_k^S}{\partial x_i}, \tag{4.8}$$

$$P_{ij}^L = -\left\langle u_j^T u_k^T \frac{\partial u_i^L}{\partial x_k} + u_i^T u_k^T \frac{\partial u_j^L}{\partial x_k} \right\rangle_{xt}, \tag{4.9}$$

$$T_{ij}^L = -\frac{\partial \langle u_i^T u_j^T u_k^L \rangle_{xt}}{\partial x_k}. \tag{4.10}$$

The derivation of the budget equation can be found in § B of the supplementary material. We note here that, because the SGS stress tensor τ_{ik}^{sgs} is a nonlinear function of the velocity, it needs to be treated as a whole to obtain $(\tau_{ik}^{sgs})^T$. Specifically, τ_{ik}^{sgs} is first calculated as a function of x, y, z and t using the dynamic Smagorinsky model (Smargorinsky 1963; Germano *et al.* 1991; Lilly 1992). The triple decomposition given by (2.6)–(2.9) is then applied to obtain $(\tau_{ik}^{sgs})^T$. Compared with the transport equations of $\langle u_i' u_j' \rangle$ (Harcourt 2013; Sinha *et al.* 2015), besides the replacement of the total velocity fluctuation u_i' by the background turbulence velocity fluctuation u_i^T in (4.1)–(4.10), the above transport equations are different from those of $\langle u_i' u_j' \rangle$ in two respects. First, there are two extra terms, P_{ij}^L and T_{ij}^L, which indicate the direct impact of the LCs on the localized Reynolds stresses. Secondly, only the time and streamwise averaging is applied in (4.1)–(4.10), so that the spanwise variation of these terms can be obtained to reveal their roles in the localization of $\langle u_i^T u_j^T \rangle_{xt}$. Similar to § 3, case 1 is used as a representation to study the transport equations of the localized Reynolds stresses. Other cases are used to examine the predictive models for the localized Reynolds stresses proposed in § 5 based on the mechanisms discussed in this section.

4.2. *Budget terms of $\langle u_i^T u_j^T \rangle_{xt}$ near the bottom*

We start the analyses of the budget balance of $\langle u_i^T u_j^T \rangle_{xt}$ with the near-bottom region first. Figure 6 shows the vertical profiles of the budget terms of $\langle u^T u^T \rangle_{xt}$ in the

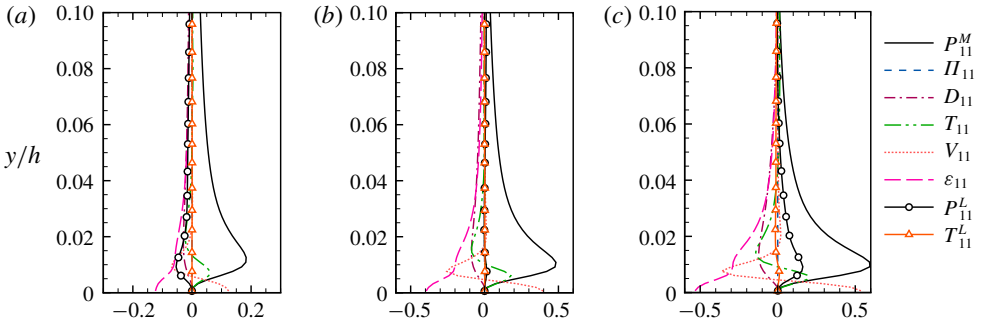

FIGURE 6. Vertical profiles of budget terms in the transport equation of $\langle u^T u^T \rangle_{xt}$ near the bottom at (*a*) UC, (*b*) HC and (*c*) DC. The results of case 1 are shown. The budget terms are scaled by u_τ^4/ν.

near-bottom region at UC, HC and DC. The dominant source of $\langle u^T u^T \rangle_{xt}$ is the mean-shear production term P_{11}^M. The expression of P_{11}^M given by (4.2) can be further simplified to

$$P_{11}^M = 2\langle -u^T v^T \rangle_{xt} \frac{\mathrm{d}\langle u \rangle}{\mathrm{d}y}. \tag{4.11}$$

Because the value of $\mathrm{d}\langle u \rangle/\mathrm{d}y$ is independent of z, the spanwise variation of P_{11}^M is completely induced by the localizing effect of the LCs on $\langle -u^T v^T \rangle_{xt}$. From the vertical profiles of $\langle -u^T v^T \rangle_{xt}$ shown in figure 3(*d*), it is known that, below $y/h = 0.03$, the magnitude of P_{11}^M is larger at DC than at HC and UC, while the magnitude of P_{11}^M at DC becomes smaller than that at HC and UC for $y/h \geqslant 0.03$ and $y/h \geqslant 0.07$, respectively. Below $y/h = 0.04$, the LC content production term P_{11}^L is another important term in the budget balance of $\langle u^T u^T \rangle_{xt}$. From figure 6, it is seen that the value of P_{11}^L is negative and positive at UC and DC, respectively. Such a spanwise variation of P_{11}^L tends to suppress and enhance the intensity of u^T in the U-region and D-region, respectively.

The combined effect of the two production terms P_{11}^M and P_{11}^L is the dominant reason that leads to the spanwise variation of $\langle u^T u^T \rangle_{xt}$. Below $y/h = 0.03$, the effects of P_{11}^M and P_{11}^L are consistent; both tend to amplify $\langle u^T u^T \rangle_{xt}$ at DC, and, as a result, the magnitude of $\langle u^T u^T \rangle_{xt}$ is larger at DC than at both UC and HC (figure 3*a*). Between $y/h = 0.03$ and 0.04, although the magnitude of P_{11}^M is slightly smaller at DC than at HC, the magnitude of $\langle u^T u^T \rangle_{xt}$ is still larger at DC due to the contribution of the positive LC content production term P_{11}^L. Above $y/h = 0.04$, the contribution of P_{11}^L is negligibly small at all of the three spanwise locations, and, consequently, the localizing effect of LCs on $\langle u^T u^T \rangle_{xt}$ is largely correlated with P_{11}^M or equivalently $\langle -u^T v^T \rangle_{xt}$ (figure 3*d*). This explains the observation from figure 3(*a*) that the magnitude of $\langle u^T u^T \rangle_{xt}$ at DC is smaller than that at HC and UC for $y/h \geqslant 0.04$ and $y/h \geqslant 0.07$, respectively.

Figure 7 shows the profiles of the budget terms in the transport equation of $\langle v^T v^T \rangle_{xt}$ at various spanwise locations in the near-bottom region. Below $y/h = 0.02$, the budget is dominated by the balance between the negative pressure–strain correlation term D_{22} and the positive pressure diffusion term Π_{22} at DC, HC and UC. The magnitude of Π_{22} is larger at DC than at HC and UC, indicating that, at DC, more energy is diffused towards the near-bottom region. As a result, the magnitude of $\langle v^T v^T \rangle_{xt}$ is larger at DC than that at HC and UC for $y/h < 0.02$.

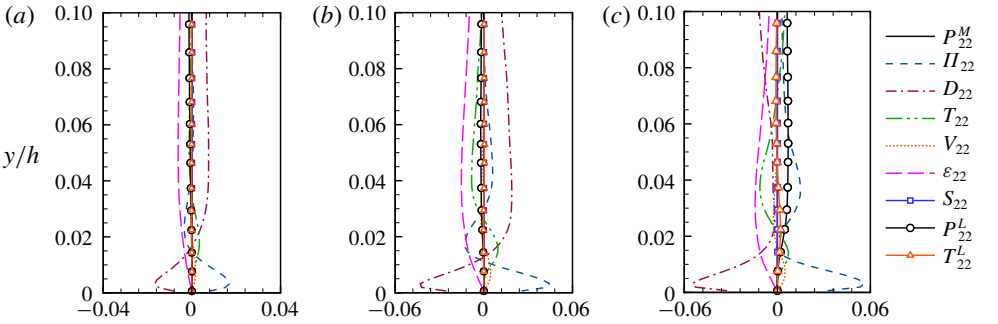

FIGURE 7. Vertical profiles of budget terms in the transport equation of $\langle v^T v^T \rangle_{xt}$ near the bottom at (*a*) UC, (*b*) HC and (*c*) DC. The results of case 1 are shown. The budget terms are scaled by u_τ^4/ν.

Above $y/h = 0.02$, the pressure–strain correlation term D_{22} is the main source of $\langle v^T v^T \rangle_{xt}$ at both UC and HC (figure 7*a*,*b*). According to the identity $D_{11} + D_{22} + D_{33} = 0$, the function of the pressure–strain correlation term is to redistribute energy among $\langle u^T u^T \rangle_{xt}$, $\langle v^T v^T \rangle_{xt}$ and $\langle w^T w^T \rangle_{xt}$ without a net production of energy. At both UC and HC, D_{11} is negative in the near-bottom region (figure 6*a*,*b*), while D_{22} is positive for $y/h > 0.02$ (figure 7*a*,*b*). This indicates that in the U-region and H-region, the vertical motion of the background turbulence, v^T, is mainly sustained by the energy redistributed from the streamwise fluctuations u^T. At UC, due to the magnitude suppression of $\langle u^T u^T \rangle_{xt}$, the energy redistributed to $\langle v^T v^T \rangle_{xt}$ is less than that at HC, such that the magnitude of $\langle v^T v^T \rangle_{xt}$ is smaller at UC than at HC (figure 3*b*).

At DC, the dominant source of $\langle v^T v^T \rangle_{xt}$ is different from that at HC and UC for $0.02 \leqslant y/h \leqslant 0.1$. As shown in figure 7(*c*), the magnitude of the pressure–strain correlation term D_{22} is small, indicating that, although the energy production of $\langle u^T u^T \rangle_{xt}$ is enhanced below $y/h = 0.04$ at DC (figure 6*c*), the energy is not gained by $\langle v^T v^T \rangle_{xt}$ through the redistribution effect of the pressure–strain correlation. Instead, the pressure diffusion term Π_{22} and the LC content production term P_{22}^L act as two dominant sources of $\langle v^T v^T \rangle_{xt}$. However, the summation of Π_{22} and P_{22}^L at DC is slightly smaller than the energy source term D_{22} at HC. As a result, the magnitude of $\langle v^T v^T \rangle_{xt}$ at DC is smaller than that at HC for $0.02 \leqslant y/h \leqslant 0.1$ (figure 3*b*).

Figure 8 compares the budget balance of $\langle w^T w^T \rangle_{xt}$ at UC, HC and DC below $y/h = 0.1$. It is seen that the pressure–strain correlation term D_{33} acts as the dominant source at all of the three spanwise locations. The positively valued D_{33} combined with the negatively valued D_{11} (figure 6) below $y/h = 0.1$ redistributes energy from u^T to w^T. The magnitude of D_{33} is smaller at UC than at HC, and is larger at DC than at HC. Correspondingly, the intensity of w^T is suppressed and enhanced in the U-region and D-region, respectively (figure 3*c*).

Figure 9 shows the vertical profiles of the budget terms of the localized Reynolds shear stress $\langle -u^T v^T \rangle_{xt}$ at UC, HC and DC below $y/h = 0.1$. The mean-shear production term P_{12}^M acts as an important source at all of the three spanwise locations. The definition of P_{12}^M can be rewritten as

$$P_{12}^M = \langle v^T v^T \rangle_{xt} \frac{\mathrm{d}\langle u \rangle}{\mathrm{d}y}, \tag{4.12}$$

which indicates that the magnitude of P_{12}^M is proportional to the localized Reynolds normal stress $\langle v^T v^T \rangle_{xt}$. Because $\langle v^T v^T \rangle_{xt}$ (figure 3*b*) and consequently P_{12}^M (figure 9*a*)

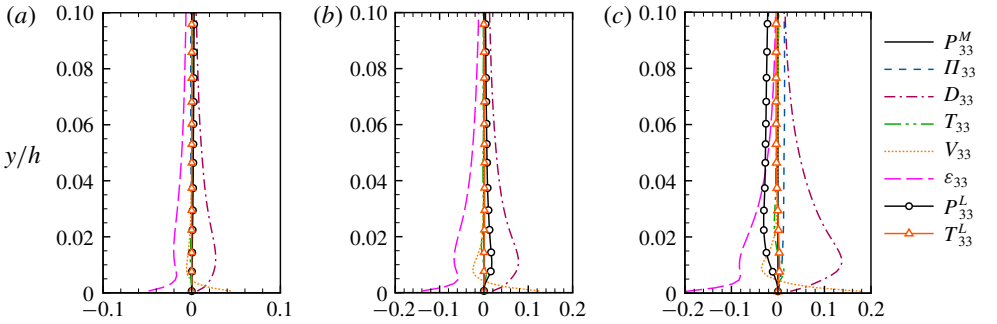

FIGURE 8. Vertical profiles of budget terms in the transport equation of $\langle w^T w^T \rangle_{xt}$ near the bottom at (*a*) UC, (*b*) HC and (*c*) DC. The results of case 1 are shown. The budget terms are scaled by u_τ^4/ν.

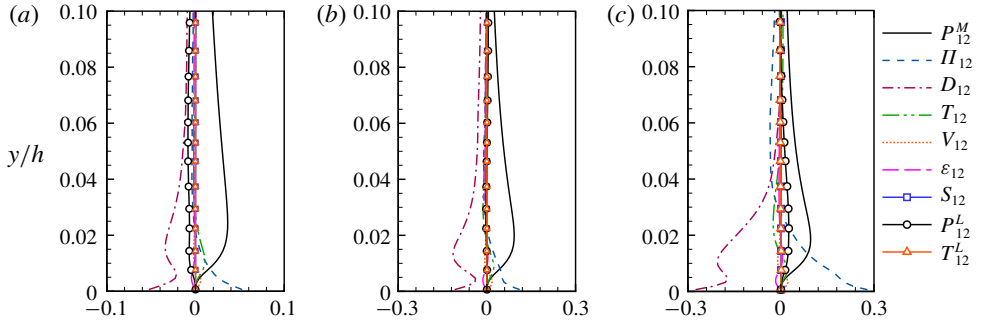

FIGURE 9. Vertical profiles of budget terms in the transport equation of $\langle -u^T v^T \rangle_{xt}$ near the bottom at (*a*) UC, (*b*) HC and (*c*) DC. The results of case 1 are shown. The budget terms are scaled by u_τ^4/ν.

are reduced at UC, $\langle -u^T v^T \rangle_{xt}$ is suppressed there. Also, from (4.12), it is understood that the magnitude of P^M_{12} is larger at HC than at DC following $\langle v^T v^T \rangle_{xt}$ (figure 3*b*). Above $y/h = 0.03$, P^M_{12} is the dominant source at both HC and DC, such that the magnitude of $\langle -u^T v^T \rangle_{xt}$ is larger at HC than at DC (figure 9*b*,*c*). Below $y/h = 0.03$, the pressure diffusion term Π_{12} acts as another important source, the magnitude of which is larger at DC than at HC. The spanwise variation of Π_{12} leads to a larger magnitude of $\langle -u^T v^T \rangle_{xt}$ at DC in comparison with that at HC for $y/h \leqslant 0.3$.

4.3. *Budget balance of* $\langle u_i^T u_j^T \rangle_{xt}$ *near the surface*

Next, we study the budget balance of the localized Reynolds stresses near the surface. Figure 10 compares the vertical profiles of the budget terms in the transport equation of $\langle u^T u^T \rangle_{xt}$ at different spanwise locations UC, HC and DC in the near-surface region for $y/h \geqslant 1.9$. The mean-shear production term P^M_{11} is the dominant source at all of the three spanwise locations. As indicated by (4.11), the magnitude of P^M_{11} is proportional to that of $\langle -u^T v^T \rangle_{xt}$. Therefore, from the comparison of $\langle -u^T v^T \rangle_{xt}$ at different spanwise locations shown in figure 4(*d*), it is understood that the magnitude of P^M_{11} is larger at DC than at HC, and smaller at UC than at HC. This is consistent with the localizing effect of LCs on the magnitude of $\langle u^T u^T \rangle_{xt}$ shown in figure 4(*a*).

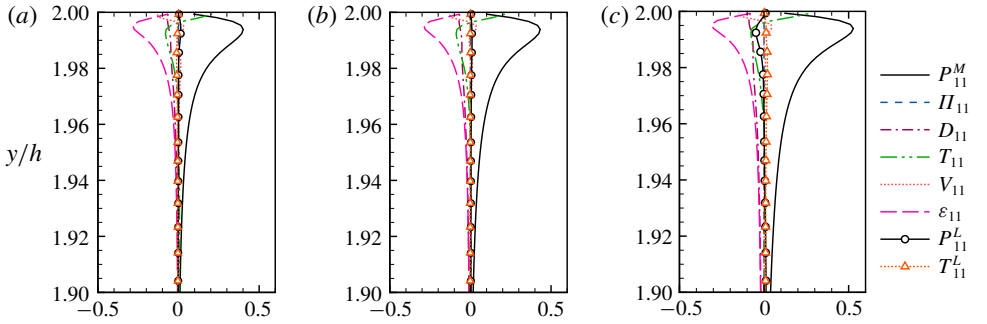

FIGURE 10. Vertical profiles of budget terms in the transport equation of $\langle u^T u^T \rangle_{xt}$ near the surface at (*a*) UC, (*b*) HC and (*c*) DC. The results of case 1 are shown. The budget terms are scaled by u_τ^4/ν.

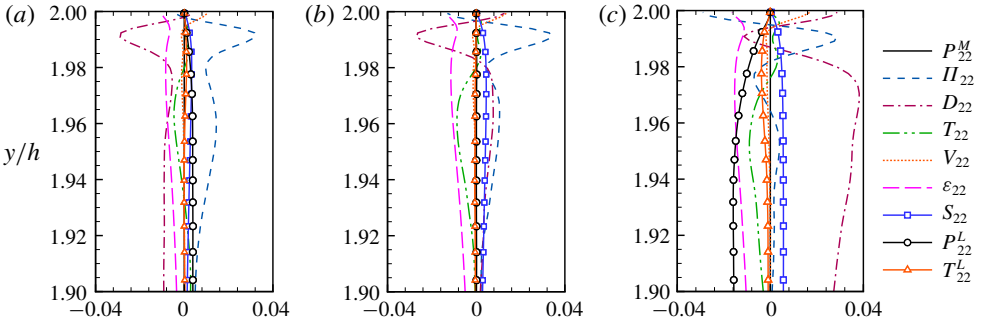

FIGURE 11. Vertical profiles of budget terms in the transport equation of $\langle v^T v^T \rangle_{xt}$ near the surface at (*a*) UC, (*b*) HC and (*c*) DC. The results of case 1 are shown. The budget terms are scaled by u_τ^4/ν.

Figure 11 compares the budget balance of $\langle v^T v^T \rangle_{xt}$ at UC, HC and DC in the near-surface region. The difference in the role of the pressure–strain correlation term D_{22} at UC, HC and DC is one of the most important mechanisms that lead to the localization of $\langle v^T v^T \rangle_{xt}$ near the surface. At UC (figure 11*a*), the value of D_{22} is negative, indicating the loss of energy of v^T through the energy redistribution. At HC (figure 11*b*), D_{22} is also negative for $y/h \geqslant 1.983$, but, as the distance from the surface increases to $y/h > 1.983$, the role of D_{22} changes to a source term of $\langle v^T v^T \rangle_{xt}$. At DC (figure 11*c*), D_{22} acts as the dominant source of $\langle v^T v^T \rangle_{xt}$ for $y/h < 1.985$, which together with the negative D_{11} (figure 10*c*) redistributes energy from $\langle u^T u^T \rangle_{xt}$ to $\langle v^T v^T \rangle_{xt}$. The magnitude of D_{22} at DC is significantly larger than all of the source terms at HC and UC. As a result, the magnitude of $\langle v^T v^T \rangle_{xt}$ is much larger at DC than at both HC and UC (figure 4*b*).

The primary source for $\langle v^T v^T \rangle_{xt}$ at UC and HC (figure 11*a*,*b*) is the pressure diffusion term Π_{22}, indicating an energy flux from the central region of the water column to the near-surface region. The magnitude of Π_{22} is comparable between UC and HC in the near-surface region of $y/h \geqslant 1.983$, while it is slightly larger at UC than at HC for $y/h < 1.983$. However, the magnitude of $\langle v^T v^T \rangle$ is slightly smaller at UC than at HC (figure 4*b*) due to the effects of the Stokes forcing term S_{22}, the LC content production term P_{22}^L and the pressure–strain correlation term D_{22}, as discussed

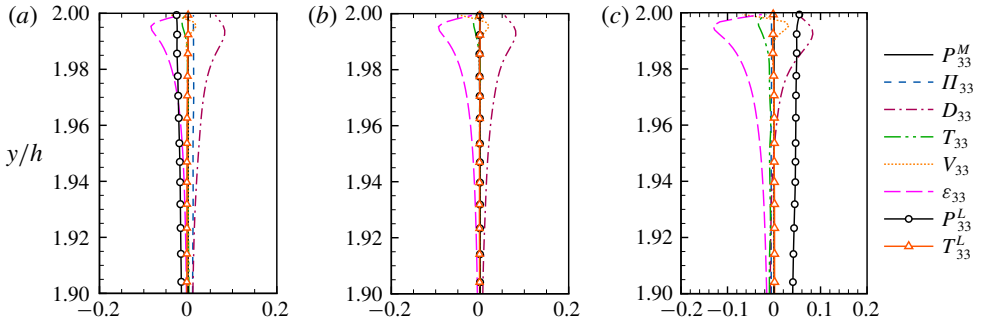

FIGURE 12. Vertical profiles of budget terms in the transport equation of $\langle w^T w^T \rangle_{xt}$ near the surface at (*a*) UC, (*b*) HC and (*c*) DC. The results of case 1 are shown. The budget terms are scaled by u_τ^4/ν.

below. Figure 11(*a*) shows that, in addition to Π_{22}, both S_{22} and P^L_{22} also act as sources at UC, while S_{22} and D_{22} feed energy to $\langle v^T v^T \rangle$ at HC (figure 11*b*). The general expression of the Stokes forcing term S_{22} given by (4.8) can be simplified to

$$S_{22} = 2\langle -u^T v^T \rangle_{xt} \frac{\mathrm{d}u^S}{\mathrm{d}y}. \tag{4.13}$$

Because u^S is homogeneous in the spanwise direction as defined in (2.4), the spanwise variation of S_{22} is induced by $\langle -u^T v^T \rangle_{xt}$, the magnitude of which is smaller at UC than at HC (figure 4*d*). In this regard, the difference in S_{22} between UC and HC is responsible for the phenomenon that the magnitude of $\langle v^T v^T \rangle_{xt}$ is slightly smaller at UC than at HC. Furthermore, the magnitude of P^L_{22} at UC is smaller than that of D^L_{22} at HC. This also tends to result in a smaller magnitude of $\langle v^T v^T \rangle$ at UC than at HC.

Figure 12 depicts the vertical profiles of the budget terms in the transport equation of $\langle w^T w^T \rangle_{xt}$ near the surface. It is seen that the pressure–strain correlation term D_{33} is an important source at all of the three spanwise locations. The magnitudes of D_{33} at UC, HC and DC are all comparable. At DC, the LC content production term P^L_{33} acts as an additional source term (figure 12*c*), which tends to enhance the intensity of w^T. As a result, the magnitude of $\langle w^T w^T \rangle_{xt}$ is larger at DC than at HC and UC (figure 4*c*). The reason for the difference in the magnitude of $\langle w^T w^T \rangle_{xt}$ between HC and UC (figure 4*c*) is complex. By contrasting the pressure–strain correlation term D_{33} and Π_{33} between HC and UC (see § C of the supplementary material), we found that D_{33} is comparable at UC and HC. Meanwhile, Π_{33} acts as a secondary source at UC, while at HC the contribution of Π_{33} in the budget balance is unimportant. The combined effects of D_{33} and Π_{33} lead to the larger magnitude of $\langle w^T w^T \rangle_{xt}$ at UC than at HC.

From the above analyses, it is understood that the localized Reynolds shear stress $\langle -u^T v^T \rangle_{xt}$ influences the localizing effects on both $\langle u^T u^T \rangle_{xt}$ and $\langle v^T v^T \rangle_{xt}$ near the surface. To further study the reason that leads to the localization of $\langle -u^T v^T \rangle_{xt}$, the vertical profiles of the budget terms of its transport equation in the near-surface region is shown in figure 13. From the figure, it is seen that the mean-shear production term P^M_{12} and Stokes forcing term S_{12} are the primary and secondary source terms, respectively. The expression for S_{12} can be simplified from the general one in (4.8) to

$$S_{12} = \langle u^T u^T \rangle_{xt} \frac{\mathrm{d}u^S}{\mathrm{d}y}. \tag{4.14}$$

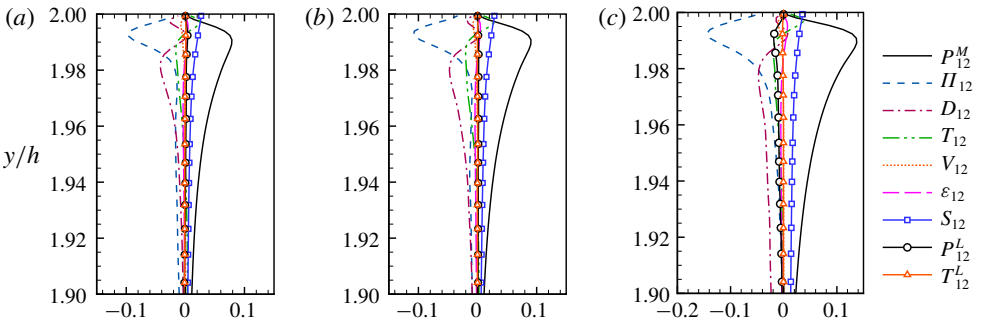

FIGURE 13. Vertical profiles of budget terms in the transport equation of $\langle -u^T v^T \rangle_{xt}$ near the surface at (*a*) UC, (*b*) HC and (*c*) DC. The results of case 1 are shown. The budget terms are scaled by u_τ^4/ν.

From (4.12) and (4.14), it is straightforward to see that, because both $\mathrm{d}\langle u \rangle/\mathrm{d}y$ and $\mathrm{d}u^S/\mathrm{d}y$ are independent of z, the spanwise variations of P_{12}^M and S_{12} are induced by $\langle v^T v^T \rangle_{xt}$ and $\langle u^T u^T \rangle_{xt}$, respectively. From the spanwise variations of $\langle u^T u^T \rangle_{xt}$ and $\langle v^T v^T \rangle_{xt}$ near the surface (figure 4*a*,*b*), it is evident that the summation of P_{12}^M and S_{12} is larger at DC and smaller at UC than at HC. The localization of the source terms P_{12}^M and S_{12} is consistent with the spanwise variation of $\langle -u^T v^T \rangle_{xt}$ observed in figure 4(*d*).

4.4. *Budgets of $\langle u_i^T u_j^T \rangle_{xt}$ in the central region of the water column*

In this section, we continue to study the transport equations of the localized Reynolds stresses in the central region of the water column. The objective is to find the dominant process responsible for the localization of the background turbulence. For this purpose, the important source terms are investigated to explain the reason for the large-magnitude $\langle u_i^T u_j^T \rangle_{xt}$ occurring in the U-region and D-region (figure 5).

Figure 14(*a*,*b*) shows the major source terms in the transport equation of $\langle u^T u^T \rangle_{xt}$, i.e. the mean-shear production term P_{11}^M and LC content production term P_{11}^L. The pressure–strain correlation term D_{11} is also plotted in figure 14(*c*), because the energy drained by D_{11} is an important source of $\langle v^T v^T \rangle_{xt}$. The LC content turbulent diffusion term T_{11}^L and its two components $T_{11}^{Ly} = -\partial \langle u^T u^T v^L \rangle_{xt}/\partial y$ and $T_{11}^{Lz} = -\partial \langle u^T u^T w^L \rangle_{xt}/\partial z$ are displayed in figure 14(*d–f*) to show the effects of the diffusion by the LCs. The terms T_{11}^{Ly} and T_{11}^{Lz} represent the diffusion induced by the vertical and spanwise motions of LCs, respectively. The isopleths of $\langle u^T u^T \rangle_{xt}$ are superimposed for comparison. Although P_{11}^M is the dominant source term near the bottom and surface (figures 6 and 10), its magnitude is relatively small in the central region of the water column (figure 14*a*). Instead, P_{11}^L acts as the dominant source of $\langle u^T u^T \rangle_{xt}$ in the lower half of the U-region and in the upper half of the D-region (figure 14*b*). Figure 14(*b*) also shows that the contour shape of P_{11}^L is similar to that of $\langle u^T u^T \rangle_{xt}$. From the comparison among the contour patterns of $\langle u^T u^T \rangle_{xt}$, P_{11}^M and P_{11}^L, it is evident that P_{11}^L is responsible for the localization of $\langle u^T u^T \rangle_{xt}$ in the central region of the water column.

Compared with the LC content production term P_{11}^L, the LC content turbulent diffusion term T_{11}^L makes a less significant contribution to the localization of $\langle u^T u^T \rangle_{xt}$. As shown, the energy provided by the spanwise convergent motions of LCs in the

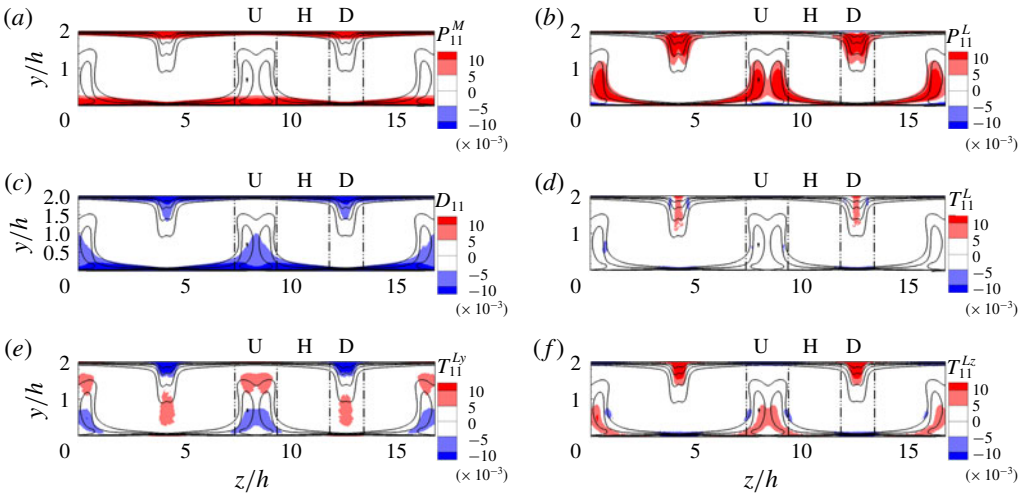

FIGURE 14. Contours of (*a*) the mean-shear production term P_{11}^M, (*b*) the LC content production term P_{11}^L, (*c*) the pressure–strain correlation term D_{11} and (*d*) the LC content turbulent diffusion term T_{11}^L and its two components (*e*) T_{11}^{Ly} and (*f*) T_{11}^{Lz} in the transport equation of $\langle u^T u^T \rangle_{xt}$ on the vertical y–z plane. These terms are scaled by u_τ^4/ν. The isopleths of $\langle u^T u^T \rangle_{xt}^+ \in [2, 5]$ with an interval of 1 are superimposed. The results of case 1 are shown.

upper half of the D-region (see T_{11}^{Lz} in figure 14*f*) is mostly diffused to the lower half of the D-region by the downwelling motions of the LCs (see T_{11}^{Ly} in figure 14*e*). As a result, the net contribution of T_{11}^L to the budget balance of $\langle u^T u^T \rangle_{xt}$ is insignificant in the upper half of the D-region, where $\langle u^T u^T \rangle_{xt}$ is enhanced due to the localizing effect of LCs. Similarly, the balance between T_{11}^{Ly} and T_{11}^{Lz} in the lower part of the U-region leads to a small net contribution of T_{11}^L to the large magnitude of $\langle u^T u^T \rangle_{xt}$ there. In the transport equations of other components of $\langle u_i^T u_j^T \rangle_{xt}$, T_{ij}^L is not the key process that leads to the localization of $\langle u_i^T u_j^T \rangle_{xt}$. As a result, they are not further analysed in the following discussions.

Figure 15 shows the important terms leading to the localization of $\langle v^T v^T \rangle_{xt}$, including the pressure–strain correlation term D_{22}, the LC content production term P_{22}^L and the Stokes forcing term S_{22}. The isopleths of $\langle v^T v^T \rangle_{xt}$ are also displayed for comparison. The value of D_{22} is positive in the lower half of the U-region and the upper half of the D-region (figure 15*a*). From the identity $D_{ii} = 0$ and the negative D_{11}, it is understood that the energy gained by $\langle v^T v^T \rangle_{xt}$ through D_{22} originates from $\langle u^T u^T \rangle_{xt}$ (figure 14*c*). As a result, the large-magnitude region of D_{22} and $\langle v^T v^T \rangle_{xt}$ collocates with that of D_{11} and $\langle u^T u^T \rangle_{xt}$. The large-magnitude contours of $\langle v^T v^T \rangle_{xt}$ in the U-region and D-region extend to the upper and lower half of the water column (figures 5*b* and 15), respectively, mainly because of the contribution of the LC content production term P_{22}^L (figure 15*b*). According to (4.9), P_{22}^L is equal to $-\langle v^T v^T \rangle_{xt} \partial \langle v^L \rangle_t / \partial y - \langle v^T w^T \rangle_{xt} \partial \langle v^L \rangle_t / \partial z$. The large-magnitude $-\langle v^T w^T \rangle_{xt}$ only occurs in the vertical centre of the D-region (figure 5*f*), and the magnitude of $\partial \langle v^L \rangle_t / \partial z$ is small near the spanwise centres of both the D- and U-regions due to the maximum magnitude of v^L there (figure 2). As a result, $-\langle v^T w^T \rangle_{xt} \partial \langle v^L \rangle_t / \partial z$ is unimportant in the budget balance of $\langle v^T v^T \rangle_{xt}$. This means that the localization of P_{22}^L is mainly caused

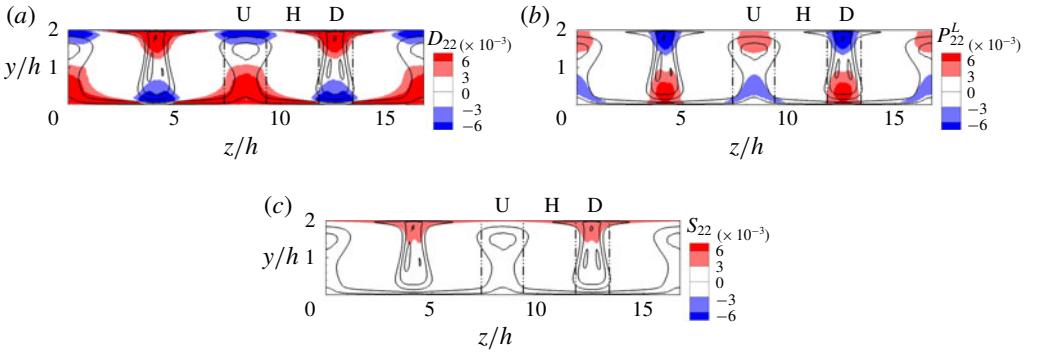

FIGURE 15. Contours of (*a*) the pressure–strain correlation term D_{22}, (*b*) the LC content production term P^L_{22} and (*c*) the Stokes forcing term S_{22} in the transport equation of $\langle v^T v^T\rangle_{xt}$ on the vertical y–z plane. These terms are normalized by u_τ^4/ν. The isopleths of $\langle v^T v^T\rangle^+_{xt} \in [0.8, 1.4]$ with an interval of 0.3 are superimposed. The results of case 1 are shown.

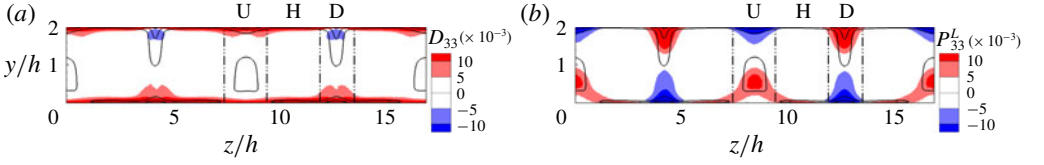

FIGURE 16. Contours of (*a*) the pressure–strain correlation D_{33} and (*b*) the LC content production term P^L_{33} in the transport equation of $\langle w^T w^T\rangle_{xt}$ on the vertical y–z plane. These terms are scaled by u_τ^4/ν. The isopleths $\langle w^T w^T\rangle^+_{xt} \in [2, 4]$ with an interval of 1 are superimposed. The results of case 1 are shown.

by $-\langle v^T v^T\rangle_{xt}\partial\langle v^L\rangle_t/\partial y$. Besides D_{22} and P^L_{22}, the Stokes forcing term S_{22} provides additional energy to $\langle v^T v^T\rangle_{xt}$ in the upper half of the D-region to enhance the intensity of v^T there (figure 15*c*). Because the vertical gradient of the Stokes drift velocity $\mathrm{d}u^S/\mathrm{d}y$ decreases as the water depth increases, the significant contribution of S_{22} to the localizing effect is confined in the upper half of the water column. According to the definition of S_{22} in (4.13), because u^S is homogeneous in the spanwise direction, the spanwise variation of $\langle -u^T v^T\rangle_{xt}$ is responsible for the localization of S_{22} in the upper half of the water column.

Figure 16 compares the contours of the two dominant source terms in the transport equation of $\langle w^T w^T\rangle_{xt}$, i.e. the pressure–strain correlation term D_{33} and the LC content production term P^L_{33}. The isopleths of $\langle w^T w^T\rangle_{xt}$ are superimposed for further investigations. The pressure–strain correlation term D_{33} only makes a significant contribution to $\langle w^T w^T\rangle_{xt}$ near the water bottom and surface, while it is insignificant in the bulk flow. This indicates that the energy redistribution process is not the dominant mechanism underlying the localization of $\langle w^T w^T\rangle_{xt}$ in the central region of the water column. The positive P^L_{33} in the lower half of the U-region and the upper half of the D-region locally contributes to the enhancement of $\langle w^T w^T\rangle_{xt}$. This is evident from the observation that the contour shape of P^L_{33} is similar to that of $\langle w^T w^T\rangle_{xt}$ (figure 16*b*). According to (4.9), P^L_{33} is equal to $-\langle v^T w^T\rangle_{xt}\partial\langle w^L\rangle_t/\partial y - \langle w^T w^T\rangle_{xt}\partial\langle w^L\rangle_t/\partial z$. Although the large-magnitude $-\langle v^T w^T\rangle_{xt}$ only occurs in the vertical centres of the D-region

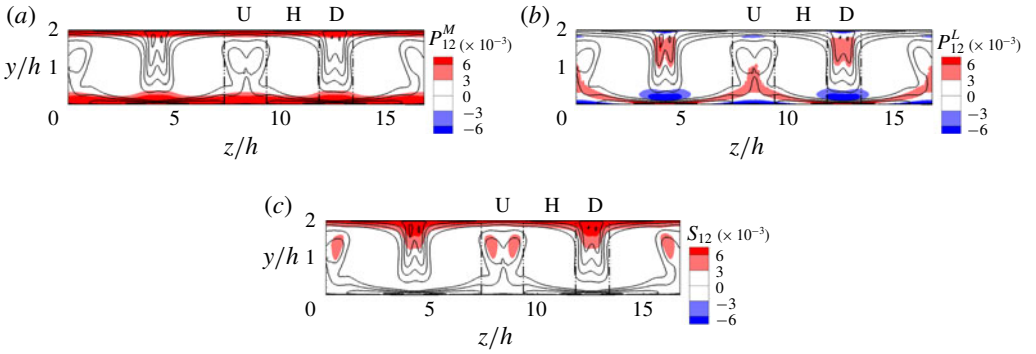

FIGURE 17. Contours of (*a*) the mean-shear production term P^M_{12}, (*b*) the LC content production term P^L_{12} and (*c*) the Stokes forcing term S_{12} in the transport equation of $\langle -u^T v^T \rangle_{xt}$ on the vertical y–z plane. These terms are scaled by u_τ^4/ν. The isopleths of $\langle -u^T v^T \rangle^+_{xt} \in [0.2, 1.2]$ with an interval of 0.25 are superimposed. The results of case 1 are shown.

(figure 5*f*), the magnitude of $\partial \langle w^L \rangle_t / \partial y$ is small near the spanwise centres of both D- and U-regions due to the small magnitude of w^L there (figure 2). As a result, $-\langle v^T w^T \rangle_{xt} \partial \langle w^L \rangle_t / \partial y$ is unimportant in the budget balance of $\langle w^T w^T \rangle_{xt}$ in the lower half of the U-region and the upper half of the D-region, though P^L_{33} is of large magnitude in these two regions. This means that the localization of P^L_{33} is mainly caused by $-\langle w^T w^T \rangle_{xt} \partial \langle w^L \rangle_t / \partial z$. Therefore, the localized distribution of $\langle w^T w^T \rangle_{xt}$ is dominated by the LC content production related to $\partial w^L / \partial z$.

The dominant source terms in the transport equation of $\langle -u^T v^T \rangle_{xt}$ are plotted in figure 17, including the mean-shear production term P^M_{12}, the LC content production term P^L_{12} and the Stokes forcing term S_{12}. As shown in figure 17(*a*), the magnitude of P^M_{12} is large near the bottom and surface; but in the central region of the water column, P^M_{12} is not the primary source in the budget balance of $\langle -u^T v^T \rangle_{xt}$. In the U-region, the LC content production term P^L_{12} is the dominant source in the lower half of the water column. The large-magnitude contours of $\langle -u^T v^T \rangle_{xt}$ in the U-region extend to the upper half of the water column (figures 5*d* and 17) mainly because of the contribution of the Stokes forcing term S_{12}. As shown in figure 17(*c*), S_{12} acts as the dominant source term between $y/h = 1.0$ and $y/h = 1.8$ in the U-region. In the D-region, S_{12} is the primary source in the upper half of the water column, while P^L_{12} works as the secondary source. According to the definition of S_{12} in (4.14), the large magnitude of S_{12} in the upper half of the D-region is due to the enhanced $\langle u^T u^T \rangle_{xt}$.

The dominant source term in the transport equation of $\langle -u^T w^T \rangle_{xt}$ is the LC content production term P^L_{13}. The contours of P^L_{13} and $\langle -u^T w^T \rangle_{xt}$ are displayed in figure 18. It is seen that the sign of P^L_{13} is consistent with that of $\langle -u^T w^T \rangle_{xt}$, and the regions with large magnitudes of P^L_{13} and $\langle -u^T w^T \rangle_{xt}$ collocate with each other. The results shown in figure 18 indicate that the LC content production is the dominant factor leading to the localization of $\langle -u^T w^T \rangle_{xt}$.

The dominant source terms in the transport equation of $\langle -v^T w^T \rangle_{xt}$ include the LC content production term P^L_{23} and the Stokes forcing term S_{23}. The contours of P^L_{23} and S_{23} are compared with those of $\langle -u^T w^T \rangle_{xt}$ in figure 19. As shown, the contours of the large-magnitude $\langle -u^T w^T \rangle_{xt}$ around the vertical centre of the D-region agree with those of P^L_{23}, while S_{23} only provides energy near the surface of the D-region. Therefore, the localization of $\langle -v^T w^T \rangle_{xt}$ is attributed to the LC content production.

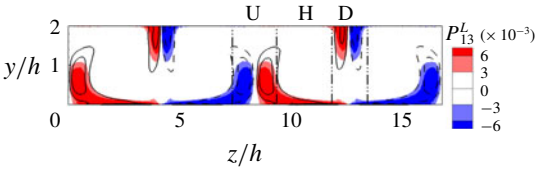

FIGURE 18. Contours of the LC content production term P^L_{13} in the transport equation of $\langle -u^T w^T \rangle$ on the vertical y–z plane. The term is normalized by u_τ^4/ν. The isopleths of $\langle -u^T w^T \rangle^+_{xt} = -1.0,\ -0.5,\ 0.5$ and 1.0 are superimposed. The solid and dashed lines represent positive and negative values of $\langle -u^T w^T \rangle_{xt}$, respectively. The results of case 1 are shown.

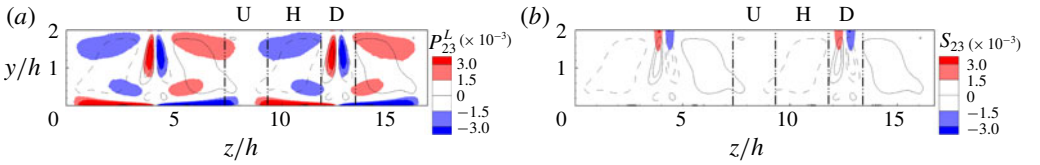

FIGURE 19. Contours of (a) the LC content production term P^L_{23} and (b) the Stokes forcing term S_{23} in the transport equation of $\langle -v^T w^T \rangle$ on the vertical y–z plane. The term is normalized by u_τ^4/ν. The isopleths of $\langle -v^T w^T \rangle^+_{xt} = -0.3,\ -0.15,\ 0.15$ and 0.3 are superimposed. The solid and dashed lines represent positive and negative values of $\langle -v^T w^T \rangle_{xt}$, respectively. The results of case 1 are shown.

In summary of the above analyses of the dominant sources in the transport equations of $\langle u_i^T u_j^T \rangle_{xt}$ in the central region of the water column, the key process responsible for the localization of $\langle u_i^T u_j^T \rangle_{xt}$ is the energy production induced by the LCs. The large magnitude of the positive LC content production in the lower half of the U-region and the upper half of the D-region (figures 14*b* and 16*b*) indicates a strong energy cascade from the large-scale LCs to small-scale background turbulence in these two regions. Kukulka *et al.* (2012) and Martinat *et al.* (2014) also studied the LC content energy production in shallow-water Langmuir turbulence. They used time and plane averaging to define statistics without considering the localizing effects. The LC content production term for $\langle u_i^T u_j^T \rangle$ (i.e. background turbulence Reynolds stresses based on time and plane averaging) obtained from their simulations is much smaller than that for $\langle u_i^T u_j^T \rangle_{xt}$ (i.e. localized Reynolds stresses without applying the spanwise averaging) obtained from the present study. The comparison between the LC content production terms in the budget balances of $\langle u_i^T u_j^T \rangle$ and $\langle u_i^T u_j^T \rangle_{xt}$ indicates that the spanwise-averaged energy cascade is much weaker than its localized counterpart. This is attributed to the fact that the LC content production for $\langle u_i^T u_j^T \rangle$ is mainly induced by the vertical gradient of the LC content velocity, $\partial u_i^L/\partial y$, while the spanwise gradient of the LC content velocity, $\partial u_i^L/\partial z$, also makes an important contribution to the energy production of the localized Reynolds stress $\langle u_i^T u_j^T \rangle$. As analysed above, the LC content production of $\langle w^T w^T \rangle$ in the central region of the water column is mainly induced by $\partial w^L/\partial z$. As further analysed in § 5, $\partial u^L/\partial z$ is essential for the LC content production of $\langle u^T u^T \rangle$ and $\langle -u^T w^T \rangle$.

5. Predictive models of localized Reynolds stresses

Based on the mechanisms underlying the localizing effects of LCs on the background turbulence discussed above, next we propose predictive models for scaling the localized Reynolds stresses and assessing the spatial dependence of Boussinesq-model parameters for localized Reynolds stresses. These models are examined in shallow-water Langmuir turbulence using the LES data with various values of the Reynolds number Re_τ, the wavenumber kh and the turbulent Langmuir number La_t.

5.1. *Near the bottom*

It is revealed in § 4.2 that the localizing effects of LCs on the magnitude of $\langle u^T u^T\rangle_{xt}$ near the bottom are attributed to the spanwise variation in the mean-shear production term P_{11}^M and LC content production term P_{11}^L. To develop the scaling of $\langle u^T u^T\rangle_{xt}$, the LC content production term P_{ij}^L in (4.9) is decomposed into two parts, P_{ij}^{Ly} and P_{ij}^{Lz}, defined as

$$P_{ij}^{Ly} = -\left\langle u_j^T u_k^T \frac{\partial u_i^L}{\partial x_k}\right\rangle_{xt}\delta_{2k} - \left\langle u_i^T u_k^T \frac{\partial u_j^L}{\partial x_k}\right\rangle_{xt}\delta_{2k} \tag{5.1}$$

and

$$P_{ij}^{Lz} = -\left\langle u_j^T u_k^T \frac{\partial u_i^L}{\partial x_k}\right\rangle_{xt}\delta_{3k} - \left\langle u_i^T u_k^T \frac{\partial u_j^L}{\partial x_k}\right\rangle_{xt}\delta_{3k}, \tag{5.2}$$

respectively, with δ_{ik} being the Kronecker delta symbol. Because u_i^L is defined using streamwise averaging and it changes little with the time (figure 1*c*), $u_i^L = \langle u_i^L\rangle_t = \langle u_i^L\rangle_{xt}$ holds approximately. As a result, P_{ij}^{Ly} and P_{ij}^{Lz} can be further simplified to

$$P_{ij}^{Ly} = -\langle u_j^T u_k^T\rangle_{xt}\frac{\partial\langle u_i^L\rangle_t}{\partial x_k}\delta_{2k} - \langle u_i^T u_k^T\rangle_{xt}\frac{\partial\langle u_j^L\rangle_t}{\partial x_k}\delta_{2k} \tag{5.3}$$

and

$$P_{ij}^{Lz} = -\langle u_j^T u_k^T\rangle_{xt}\frac{\partial\langle u_i^L\rangle_t}{\partial x_k}\delta_{3k} - \langle u_i^T u_k^T\rangle_{xt}\frac{\partial\langle u_j^L\rangle_t}{\partial x_k}\delta_{3k}, \tag{5.4}$$

respectively.

Figure 20 compares the profiles of P_{11}^L, P_{11}^{Ly} and P_{11}^{Lz} at UC, HC and DC. As shown, at all of the three spanwise locations, the profiles of P_{11}^L and P_{11}^{Ly} almost collapse, while the magnitude of P_{11}^{Lz} is negligibly small, indicating that, near the bottom, the LC content production is dominated by the interaction between $\partial\langle u^L\rangle_t/\partial y$ and $\langle -u^T v^T\rangle_{xt}$. The negative P_{11}^{Ly} near the bottom of UC implies the localized energy inverse cascade from the small-scale background turbulence to large-scale LCs. Despite the negative P_{11}^{Ly} at UC, as shown in the work of Kukulka *et al.* (2012) and Martinat *et al.* (2014), the time- and plane-averaged P_{11}^{Ly} is still positive, indicating the net energy cascade from large-scale LCs to small-scale background turbulence near the bottom.

Combining (4.11) and (5.3), a total localized production term of $\langle u^T u^T\rangle_{xt}$ can be written as

$$P_{11} = P_{11}^M + P_{11}^{Ly} = 2\langle -u^T v^T\rangle_{xt}\frac{\partial\langle u\rangle_{xt}}{\partial y}, \tag{5.5}$$

where $\langle u\rangle_{xt} = \langle u\rangle + u^L$ is the localized mean streamwise velocity defined in the same way as the localized Reynolds stress in (2.13). Near the bottom of the D-region,

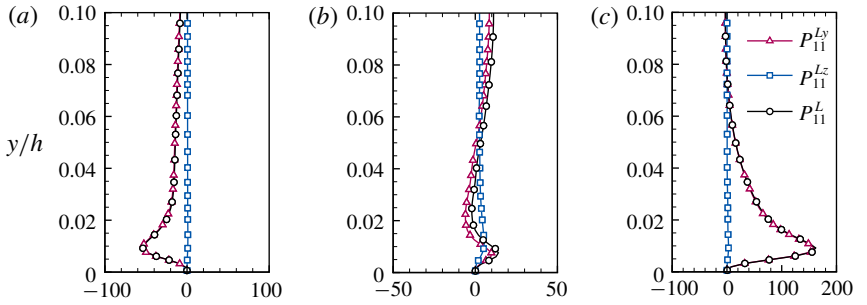

FIGURE 20. Vertical profiles of P_{11}^{Ly}, P_{11}^{Lz} and P_{11}^{L} in the near-bottom region at (*a*) UC, (*b*) HC and (*c*) DC. Here, P_{11}^{Ly}, P_{11}^{Lz} and P_{11}^{L} are scaled by u_τ^4/ν. The results of case 1 are shown.

the LC content mean velocity u^L is positive (figure 2), such that the localized mean velocity $\langle u\rangle_{xt}$ and its vertical gradient $\partial\langle u\rangle_{xt}/\partial y$ are larger than the time- and plane-averaged counterparts $\langle u\rangle$ and $\mathrm{d}\langle u\rangle/\mathrm{d}y$, respectively. In contrast, near the bottom of the U-region, the magnitudes of $\langle u\rangle_{xt}$ and $\partial\langle u\rangle_{xt}/\partial y$ are smaller than those of $\langle u\rangle$ and $\mathrm{d}\langle u\rangle/\mathrm{d}y$, respectively.

The difference in the localized mean velocity gradient indicates that the localized friction Reynolds number also varies in the spanwise direction. In canonical wall turbulence without LCs, it has been found that the profiles of near-bottom $\langle u^T u^T\rangle$ scaled by the friction velocity in the vertical coordinate normalized by wall units are insensitive to the friction Reynolds number (Smith, McKeon & Marusic 2011). In view of this, a localized friction velocity is defined as

$$u_l = \sqrt{\nu\left(\frac{\partial\langle u\rangle_{xt}}{\partial y}\right)_{y=0}}. \tag{5.6}$$

Correspondingly, a localized viscous length scale is defined as

$$\delta_l = \nu/u_l. \tag{5.7}$$

The variables normalized using u_l and δ_l are denoted by the superscript 'l'. Figure 21 compares the profiles of $\langle u^T u^T\rangle_{xt}^{+}$ in the coordinate y/h and $\langle u^T u^T\rangle_{xt}^{l}$ in the localized near-bottom coordinate y^l. The results of cases 1–4 are displayed to examine the effectiveness of the proposed scaling under various flow conditions. The profiles of time- and plane-averaged Reynolds stress $\langle u^T u^T\rangle^{+}$ for the corresponding case and shear-driven turbulent flow (case 5) are superimposed for comparison. As shown in figure 21(*a*1–4), the localizing effects of the LCs on the magnitude of $\langle u^T u^T\rangle^{+}$ in all cases are consistent. Specifically, the magnitude of $\langle u^T u^T\rangle^{+}$ is larger at DC than at HC and is smaller at UC than at HC. In contrast, figure 21(*b*1–4) shows that the profiles of $\langle u^T u^T\rangle^{l}$ at different spanwise locations collapse in the localized near-bottom coordinate y^l. They are also close to the profile of $\langle u^T u^T\rangle^{+}$ in the global near-bottom coordinate yu_τ/ν in the shear-driven turbulence. This indicates that, in the near-bottom region, the profiles of $\langle u^T u^T\rangle_{xt}^{+}$ in Langmuir turbulence under various flow conditions can be predicted using the results in the shear-driven turbulence with proper scalings.

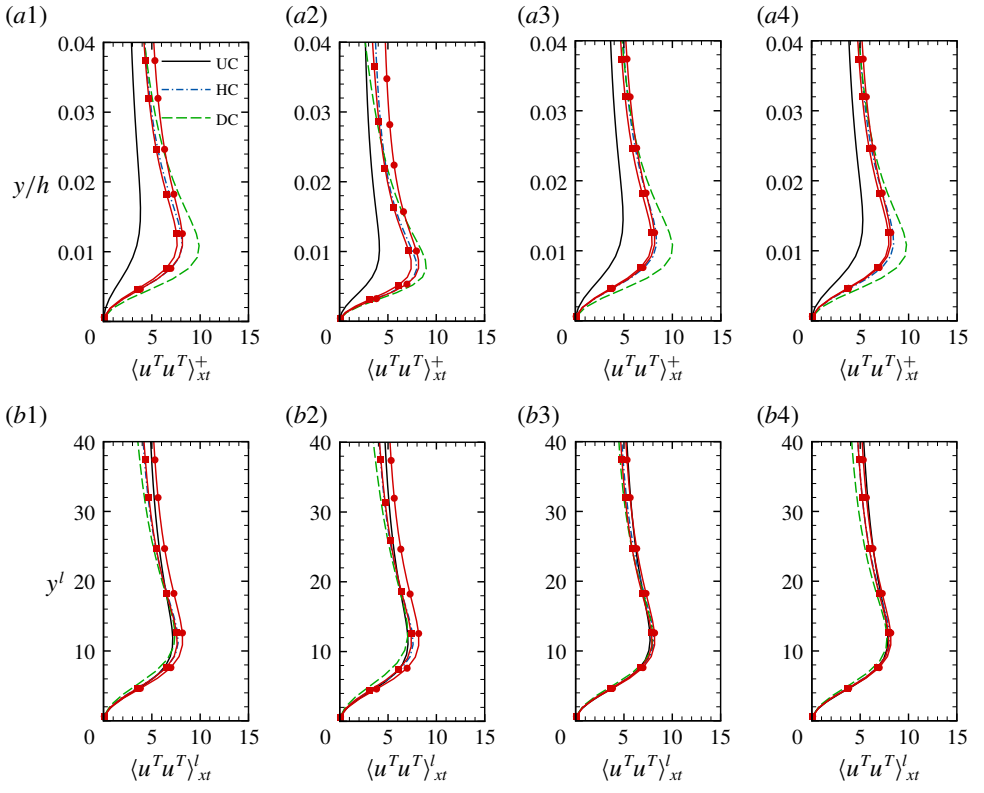

FIGURE 21. Profiles of $(a1\text{–}4)\langle u^T u^T\rangle^+_{xt}$ in the coordinate y/h and $(b1\text{–}4)$ $\langle u^T u^T\rangle^l_{xt}$ in the localized near-bottom coordinate y^l: $(a1,b1)$ $Re_\tau = 1000$, $kh = 0.5$ and $La_t = 0.7$; $(a2,b2)$ $Re_\tau = 700$, $kh = 0.5$ and $La_t = 0.7$; $(a3,b3)$ $Re_\tau = 1000$, $kh = 1.0$ and $La_t = 0.7$; and $(a4,b4)$ $Re_\tau = 1000$, $kh = 0.5$ and $La_t = 0.9$. The red lines with square symbols are the time- and plane-averaged Reynolds stress $\langle u^T u^T\rangle$ in each case, and the red lines with circle symbols are $\langle u^T u^T\rangle$ in the shear-driven turbulent flow.

To date, no scaling has been found for the profiles of $\langle v^T v^T\rangle$ and $\langle w^T w^T\rangle$ near the bottom at various Reynolds numbers in canonical wall-bounded turbulent flows (Smith *et al.* 2011; Bernardini, Pirozzoli & Orlandi 2014; Deng *et al.* 2016). The main reason is that the dominant energy sources of $\langle v^T v^T\rangle$ and $\langle w^T w^T\rangle$ are the pressure–strain correlation terms, which are challenging to model (Hoyas & Jiménez 2008). Similarly, in the Langmuir turbulence, we do not find a good scaling for $\langle v^T v^T\rangle_{xt}$ and $\langle w^T w^T\rangle_{xt}$.

For $\langle u_i^T u_j^T\rangle_{xt}$ near the surface, it is also difficult to find a simple scaling directly related to the vertical gradient of the local streamwise mean velocity at the surface in a way similar to $\langle u^T u^T\rangle_{xt}$ near the bottom. Owing to the surface boundary condition, the vertical gradient of the local mean velocity at the surface is zero, which cannot be used to present the localized distribution of $\langle u_i^T u_j^T\rangle_{xt}$ near the surface. Moreover, as analysed in § 4.3, the LC content production terms have no significant impacts on the localization of $\langle u^T u^T\rangle_{xt}$ (figure 10) and $\langle -u^T v^T\rangle_{xt}$ (figure 13) near the surface, so that the scaling related to u_i^L does not work for $\langle u^T u^T\rangle_{xt}$ and $\langle -u^T v^T\rangle_{xt}$ near the surface. For $\langle v^T v^T\rangle_{xt}$ (figure 11) and $\langle w^T w^T\rangle_{xt}$ (figure 12) near the surface, their localized distributions are related to the pressure–strain correlation terms, which are difficult to scale (Hoyas & Jiménez 2008).

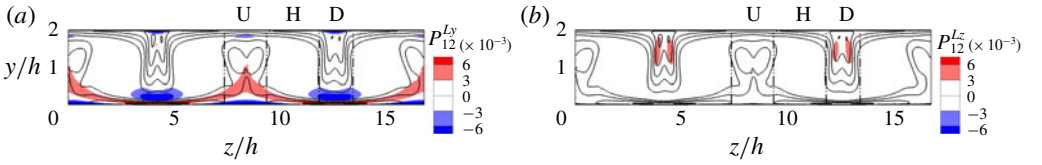

FIGURE 22. Contours of (*a*) P_{12}^{Ly} and (*b*) P_{12}^{Lz} scaled by u_τ^4/ν on the vertical y–z plane. The isopleths of $\langle -u^T v^T \rangle_{xt}^+ \in [0.2, 1.2]$ with an interval of 0.25 are superimposed. The results of case 1 are shown.

5.2. *Central region*

To develop a model for predicting the localizing effect of LCs on the localized Reynolds stresses in the central region of the water column, we first express the difference between the localized Reynolds stresses and the time- and plane-averaged Reynolds shear stresses as

$$d_{ij} = \langle -u_i^T u_j^T \rangle_{xt} - \langle -u_i^T u_j^T \rangle. \tag{5.8}$$

The spanwise averaging of d_{ij} is equal to zero. As noted by Martinat *et al.* (2014), d_{ij} is important for solving $\langle u_i \rangle_{xt}$ in RANS. According to the analyses in § 4.4, it is desirable to develop predictive models of d_{12}, d_{13} and d_{23} using the gradients of u_i^L.

The following model is proposed to predict d_{12}:

$$d_{12}^m = a_{12}\frac{\partial \langle u^L \rangle_t}{\partial y} + b_{12}\frac{\mathrm{d}u^S}{\mathrm{d}y}\frac{\partial \langle u^L \rangle_t}{\partial y} + c_{12}\frac{\mathrm{d}u^S}{\mathrm{d}y}\left(\left|\frac{\partial \langle u^L \rangle_t}{\partial z}\right| - \left\langle\left|\frac{\partial \langle u^L \rangle_t}{\partial z}\right|\right\rangle_z\right), \tag{5.9}$$

where the parameter a_{12} works as an eddy viscosity, while the dimensions of b_{12} and c_{12} are the square of length. The superscript 'm' represents d_{12} obtained from the proposed model. Here, $\langle\cdot\rangle_z$ represents the spanwise averaging. Below are the physical explanations to this model.

It is revealed in § 4.4 that the localization of $\langle -u^T v^T \rangle_{xt}$ in the lower half of the water column is attributed to the LC content production term P_{12}^L. Figure 22 compares the distributions of P_{12}^{Ly} and P_{12}^{Lz}. As shown, P_{12}^{Lz} is negligibly small compared with P_{12}^{Ly} in the lower half of the water column. From (5.3), it is understood that P_{12}^{Ly} is approximately equal to $\langle v^T v^T \rangle_{xt} \partial \langle u^L \rangle_t / \partial y + \langle u^T v^T \rangle_{xt} \partial \langle v^L \rangle_t / \partial y$. Additionally, the magnitude of $\partial \langle u^L \rangle_t / \partial y$ is larger than that of $\partial \langle v^L \rangle_t / \partial y$. Therefore, the first term on the right-hand side of (5.9) proportional to $\partial \langle u^L \rangle_t / \partial y$ is used to predict the contribution of P_{12}^{Ly} to the localization of $\langle -u^T v^T \rangle_{xt}$.

The localization of $\langle -u^T v^T \rangle_{xt}$ in the upper half of the water column is attributed to the Stokes forcing term S_{12}, which is captured using the last two terms on the right-hand side of (5.9) in the proposed model. Below are the explanations to these two terms. According to the definition of S_{12} given by (4.14), its value is determined by $\mathrm{d}u^S/\mathrm{d}y$ and $\langle u^T u^T \rangle_{xt}$, from which it is understood that it is crucial to capture the localizing effect of LCs on $\langle u^T u^T \rangle_{xt}$ in the model of $\langle -u^T v^T \rangle_{xt}$. The contours of the dominant source terms of $\langle u^T u^T \rangle_{xt}$ shown in figure 14 indicate that, in the central region of the water column, the localization of $\langle u^T u^T \rangle_{xt}$ is correlated to the LC content production term P_{11}^L. According to (5.1) and (5.2), P_{11}^L can be further decomposed into two parts, P_{11}^{Ly} and P_{11}^{Lz}, the contours of which are displayed in figure 23. As shown, both P_{11}^{Ly} and P_{11}^{Ly} are important sources of $\langle u^T u^T \rangle_{xt}$ in the upper half of the

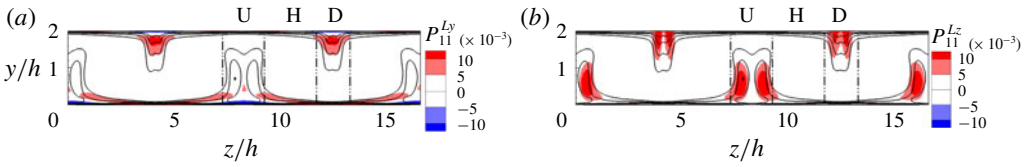

FIGURE 23. Contours of (*a*) P_{11}^{Ly} and (*b*) P_{11}^{Lz} on the vertical y–z plane. The terms are scaled by u_τ^4/ν. The isopleths of $\langle u^T u^T\rangle_{xt}^+ \in [2, 5]$ with an interval of 1 are superimposed. The results of case 1 are shown.

water column. From the simplified form of P_{11}^{Ly} given by (5.3), it is understood that $\partial\langle u^L\rangle_t/\partial y$ needs to be considered to model the effect of S_{12}. Furthermore, P_{11}^{Lz} can be approximated as $2\langle -u^T w^T\rangle_{xt}\partial\langle u^L\rangle_t/\partial z$ according to (5.4). It is shown below that the localization of $\langle -u^T w^T\rangle_{xt}$ is correlated to the spanwise gradient of the LC content streamwise velocity, $\partial\langle u^L\rangle_t/\partial z$, and as such the absolute value of $\partial\langle u^L\rangle_t/\partial z$ is used in the proposed model of $\langle -u^T v^T\rangle_{xt}$. Because the spanwise averaging of $|\partial\langle u^L\rangle_t/\partial z|$ is non-trivial, its spanwise-averaged value $\langle|\partial\langle u^L\rangle_t/\partial z|\rangle_z$ needs to be subtracted to satisfy the condition that the spanwise averaging of d_{12}^m is zero. Because the gradients of v^L and w^L have negligible contribution to the LC content production that dominates the localization of $\langle -u^T v^T\rangle_{xt}$, and because the LC content diffusion terms related to v^L and w^L are not responsible for the localization of $\langle -u^T v^T\rangle_{xt}$ (see the analysis in § 4.4), v^L and w^L are not included in the model (5.9).

In the proposed model (5.9), the parameters a_{12}, b_{12} and c_{12} are determined by minimizing the norm of the error $t_{12} = d_{12}^m - d_{12}$ in the central region $(0.1 < y/h < 1.9)$. The norm of t_{ij} is defined as

$$\|t_{ij}\| = \left(\frac{1}{1.8hL_z}\int_{y=0.1h}^{y=1.9h}\int_{z=0}^{z=L_z}|t_{ij}|^2\,\mathrm{d}y\,\mathrm{d}z\right)^{1/2}. \tag{5.10}$$

To show the performance of the model in (5.9), $\langle -u^T v^T\rangle_{xt}$ estimated by $d_{12}^m + \langle -u^T v^T\rangle$, denoted as $\langle -u^T v^T\rangle_{xt}^m$, is compared with $\langle -u^T v^T\rangle_{xt}$ obtained from the LES in figure 24. The results of cases 1–4 are all displayed to show the effectiveness of the proposed model under different flow conditions with various values of Re_τ, kh and La_t. As shown, the spatial variation of $\langle -u^T v^T\rangle_{xt}$ is in general captured by the proposed model in all of the four cases. The performance of the model is further examined quantitatively using the values of $\|t_{12}\|$ and the correlation coefficient between $\langle -u^T v^T\rangle_{xt}^m$ and $\langle -u^T v^T\rangle_{xt}$ defined as

$$C = \frac{\displaystyle\int_{y=0}^{y=1.9h}\int_{z=0}^{z=L_z}\langle -u^T v^T\rangle_{xt}^m\langle -u^T v^T\rangle_{xt}\,\mathrm{d}y\,\mathrm{d}z}{1.8hL_z\|\langle -u^T v^T\rangle_{xt}^m\|\,\|\langle -u^T v^T\rangle_{xt}\|}. \tag{5.11}$$

As listed in figure 24(*a*2,*b*2,*c*2,*d*2), the value of $\|t_{12}\|$ is small in all cases compared with the amplitude of $\langle -u^T v^T\rangle_{xt}$, and the correlation coefficient is larger than 0.7, indicating that the dominant mechanism underlying the localization of $\langle -u^T v^T\rangle_{xt}$ is captured by the proposed model.

To develop a model for $\langle -u^T w^T\rangle_{xt}$, its dominant source term P_{13}^L is decomposed into P_{13}^{Ly} and P_{13}^{Lz}, the contours of which are displayed in figure 25. As shown,

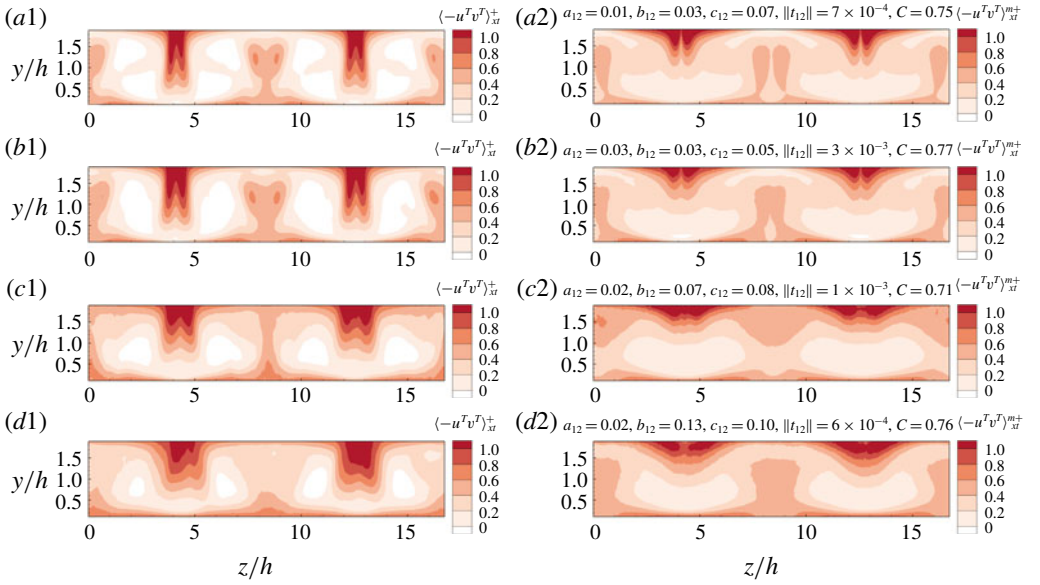

FIGURE 24. Comparison of $\langle -u^T v^T\rangle_{xt}^{+}$ with $\langle -u^T v^T\rangle_{xt}^{m+}$ in the central region ($0.1 < y/h < 1.9$): (*a*1,*b*1,*c*1,*d*1) $\langle -u^T v^T\rangle_{xt}^{+}$ obtained from the LES and (*a*2,*b*2,*c*2,*d*2) the estimated $\langle -u^T v^T\rangle_{xt}^{m+}$ using (5.9); (*a*1,*a*2) $Re_\tau = 1000$, $kh = 0.5$ and $La_t = 0.7$; (*b*1,*b*2) $Re_\tau = 700$, $kh = 0.5$ and $La_t = 0.7$; (*c*1,*c*2) $Re_\tau = 1000$, $kh = 1.0$ and $La_t = 0.7$; and (*d*1,*d*2) $Re_\tau = 1000$, $kh = 0.5$ and $La_t = 0.9$.

due to the negligible magnitude of P_{13}^{Ly}, the distribution of P_{13}^{L} is dominated by P_{13}^{Lz}. According to (5.4), P_{13}^{Lz} can be approximated as $\langle w^T w^T\rangle_{xt}\partial\langle u^L\rangle_t/\partial z + \langle u^T w^T\rangle_{xt}\partial\langle w^L\rangle_t/\partial z$. Because the magnitudes of $\langle u^T w^T\rangle_{xt}$ and $\partial\langle w^L\rangle_t/\partial z$ are much smaller than those of $\langle w^T w^T\rangle_{xt}$ and $\partial\langle u^L\rangle_t/\partial z$, respectively, P_{13}^{Lz} is dominated by $\langle w^T w^T\rangle_{xt}\partial\langle u^L\rangle_t/\partial z$. The significant discrepancy between the distribution of P_{13}^{Lz} (figure 25*b*) and that of $\langle w^T w^T\rangle_{xt}$ (figure 5*c*) further indicates that $\partial\langle u^L\rangle_t/\partial z$ dominates the localization of P_{13}^{Lz}. Therefore, it is crucial to involve $\partial\langle u^L\rangle_t/\partial z$ in the model of $\langle -u^T w^T\rangle_{xt}$. Based on the above analysis, the model of d_{13} is proposed as

$$d_{13}^{m} = a_{13}\frac{\partial\langle u^L\rangle_t}{\partial z}. \tag{5.12}$$

Here, a_{13} has the dimension of viscosity, which is obtained by minimizing the norm of $t_{13} = d_{13}^{m} - d_{13}$. Similar to the model (5.9), v^L and w^L are not included, because the LC content production related to them and the diffusion induced by them are insignificant to the localization of $\langle -u^T w^T\rangle_{xt}$. Figure 26 compares $\langle -u^T w^T\rangle_{xt}^{m} = d_{13}^{m} + \langle -u^T w^T\rangle$ with $\langle -u^T w^T\rangle_{xt}$. The correlation coefficient between $\langle -u^T w^T\rangle_{xt}^{m}$ and $\langle -u^T w^T\rangle_{xt}$ in figure 26 is defined in the same manner as given by (5.11). In all cases, the correlation coefficient is larger than 0.9, and the value of $\|t_{13}\|$ is much smaller than the magnitude of $\langle -u^T w^T\rangle_{xt}$, indicating a satisfactory performance of the proposed model.

The correlation coefficient between $\langle -u^T w^T\rangle_{xt}^{m}$ and $\langle -u^T w^T\rangle_{xt}$ is much larger than that between $\langle -u^T v^T\rangle_{xt}^{m}$ and $\langle -u^T v^T\rangle_{xt}$. This is related to the relatively complex physical processes leading to the localization of $\langle -u^T v^T\rangle_{xt}$. The model (5.12) for $\langle -u^T w^T\rangle_{xt}$ accounts for the sole process represented by P_{13}^{Lz} that dominates the

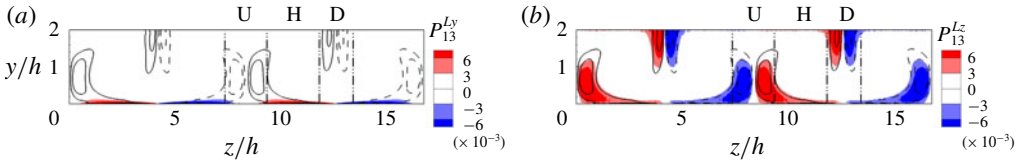

FIGURE 25. Contours of (*a*) P_{13}^{Ly} and (*b*) P_{13}^{Lz} on the vertical y–z plane. The terms are scaled by u_τ^4/ν. The isopleths of $\langle -u^T w^T \rangle_{xt} = -1.0$, -0.5, 0.5 and 1.0 are superimposed. The solid and dashed lines represent positive and negative values of $\langle -u^T w^T \rangle_{xt}$. The results of case 1 are shown.

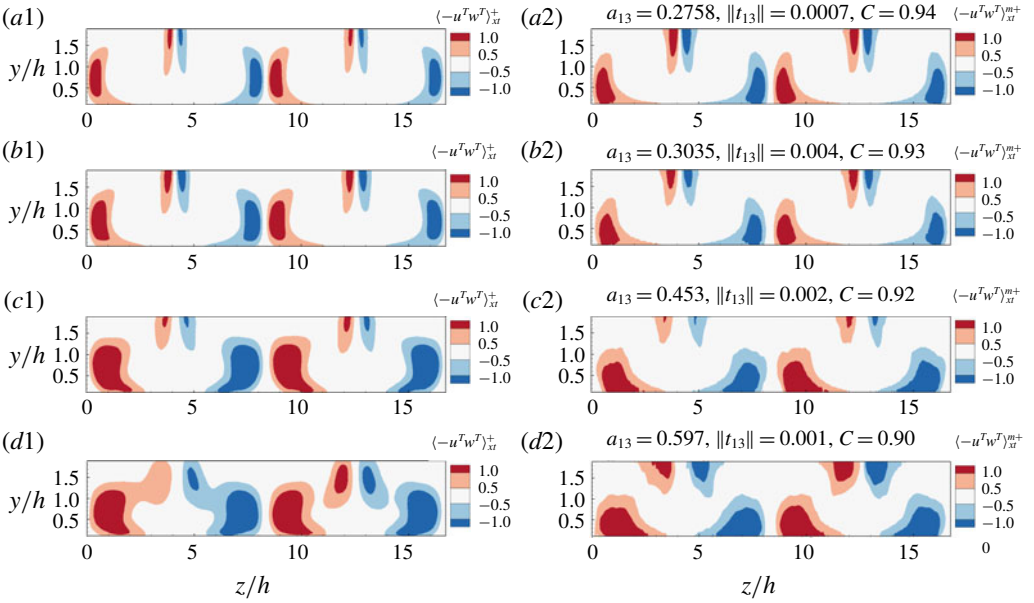

FIGURE 26. Comparison between $\langle -u^T w^T \rangle_{xt}^{+}$ with the modelled one $\langle -u^T w^T \rangle_{xt}^{m+}$ in the central region ($0.1 < y/h < 1.9$): (*a*1,*b*1,*c*1,*d*1) $\langle -u^T w^T \rangle_{xt}^{+}$ obtained from the LES and (*a*2,*b*2,*c*2,*d*2) $\langle -u^T w^T \rangle_{xt}^{m+}$ estimated using (5.12); (*a*1,*a*2) $Re_\tau = 1000$, $kh = 0.5$ and $La_t = 0.7$; (*b*1,*b*2) $Re_\tau = 700$, $kh = 0.5$ and $La_t = 0.7$; (*c*1,*c*2) $Re_\tau = 1000$, $kh = 1.0$ and $La_t = 0.7$; and (*d*1,*d*2) $Re_\tau = 1000$, $kh = 0.5$ and $La_t = 0.9$.

localization of $\langle -u^T w^T \rangle_{xt}$, so that the correlation coefficient between $\langle -u^T w^T \rangle_{xt}^{m}$ and $\langle -u^T w^T \rangle_{xt}$ is relatively high. In contrast, the localization of $\langle -u^T v^T \rangle_{xt}$ is induced by different physical processes in different regions. The term P_{12}^{Ly} related to $\partial u^L/\partial y$ is responsible for the strong $\langle -u^T v^T \rangle_{xt}$ in the U-region, and the Stokes forcing term related to $\mathrm{d}u^S/\mathrm{d}y$ leads to the intensified $\langle -u^T v^T \rangle_{xt}$ in the D-region. However, P_{12}^{Ly} acts to reduce the intensity of $\langle -u^T v^T \rangle_{xt}$ between $0.15 < y/h < 0.45$ in the D-region (figure 23*a*). Therefore, the contours of high-intensity $\langle -u^T v^T \rangle_{xt}^{m}$ in the D-region cannot penetrate as deep as those of $\langle -u^T v^T \rangle_{xt}$, which leads to a relatively smaller correlation coefficient between $\langle -u^T v^T \rangle_{xt}^{m}$ and $\langle -u^T v^T \rangle_{xt}$.

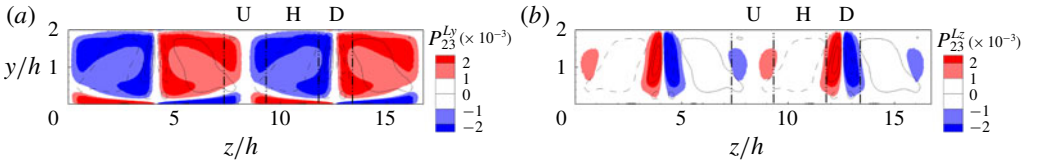

FIGURE 27. Contours of (*a*) P_{23}^{Ly} and (*b*) P_{23}^{Lz} on the vertical y–z plane. The terms are scaled by u_τ^4/ν. The isopleths of $\langle -v^T w^T\rangle_{xt} = -0.3$, -0.15, 0.15 and 0.3 are superimposed. The solid and dashed lines represent positive and negative values of $\langle -v^T w^T\rangle_{xt}$. The results of case 1 are shown.

For $\langle -v^T w^T\rangle_{xt}$, its dominant source term P_{23}^L can be simplified as

$$\begin{aligned} P_{23}^L &= -\langle v^T w^T\rangle_{xt}\frac{\partial\langle v^L\rangle_t}{\partial y} - \langle v^T v^T\rangle_{xt}\frac{\partial\langle w^L\rangle_t}{\partial y} - \langle w^T w^T\rangle_{xt}\frac{\partial\langle v^L\rangle_t}{\partial z} - \langle v^T w^T\rangle_{xt}\frac{\partial\langle w^L\rangle_t}{\partial z} \\ &= -\langle v^T v^T\rangle_{xt}\frac{\partial\langle w^L\rangle_t}{\partial y} - \langle w^T w^T\rangle_{xt}\frac{\partial\langle v^L\rangle_t}{\partial z}, \end{aligned} \tag{5.13}$$

because $-\partial v^L/\partial y - \partial w^L/\partial z = \partial u^L/\partial x$ is equal to zero according to the definition of u_i^L in (2.8). The components P_{23}^{Ly} and P_{23}^{Lz} are equal to $-\langle v^T v^T\rangle_{xt}\partial\langle w^L\rangle_t/\partial y$ and $-\langle w^T w^T\rangle_{xt}\partial\langle v^L\rangle_t/\partial z$, respectively, the contours of which are shown in figure 27. It is seen that P_{23}^{Ly} is responsible for the localized distribution of $\langle -v^T w^T\rangle_{xt}$ in the H-region, while P_{23}^{Lz} is responsible for the large magnitude of $\langle -v^T w^T\rangle_{xt}$ in the D-region. Therefore, $\partial\langle v^L\rangle_t/\partial z$ and $\partial\langle w^L\rangle_t/\partial y$ are involved in the model of $\langle -v^T w^T\rangle_{xt}$, which is written as

$$d_{23}^m = a_{23}\frac{\partial\langle w^L\rangle_t}{\partial y} + b_{23}\frac{\partial\langle v^L\rangle_t}{\partial z}. \tag{5.14}$$

Similar to a_{13} in (5.12), a_{23} and b_{23} have the dimension of viscosity, and are determined by minimizing the norm of $t_{23} = d_{23}^m - d_{23}$. Figure 28 compares $\langle -v^T w^T\rangle_{xt}^m = d_{23}^m + \langle -v^T w^T\rangle$ with $\langle -v^T w^T\rangle_{xt}$. The norm of the error t_{23} is negligibly small in comparison with the magnitude of $\langle -v^T w^T\rangle_{xt}$, and the correlation coefficient between $\langle -v^T w^T\rangle_{xt}^m$ and $\langle -v^T w^T\rangle_{xt}$ is approximately 0.8.

In comparison with the traditional eddy-viscosity model of the Reynolds stresses, the above three models are different in two respects. First, the Reynolds shear stress in the traditional model is related to the mean strain rate, but the model for d_{ij} is related to the localized velocity gradient $\partial u_i^L/\partial x_j$ to reflect the localizing effect of the LCs on the background turbulence. This indicates that the Boussinesq-model parameters for the localized Reynolds stresses are spatially dependent. The adoption of the localized velocity gradient guarantees that the spanwise averaging of d_{ij}^m is zero. Secondly, the gradient of the Stokes drift velocity is also taken into account in the proposed model of $\langle -u^T v^T\rangle_{xt}$. This is due to the feature of Langmuir turbulence that the energy extracted from the shear of the Stokes drift velocity makes considerable contributions to $\langle -u^T v^T\rangle_{xt}$. For the purpose of the application of the model, further efforts are needed to parametrize the coefficients. This will rely on a large amount of data from field measurements and numerical simulations. Once more data are available in the future, it will be straightforward to determine the coefficients.

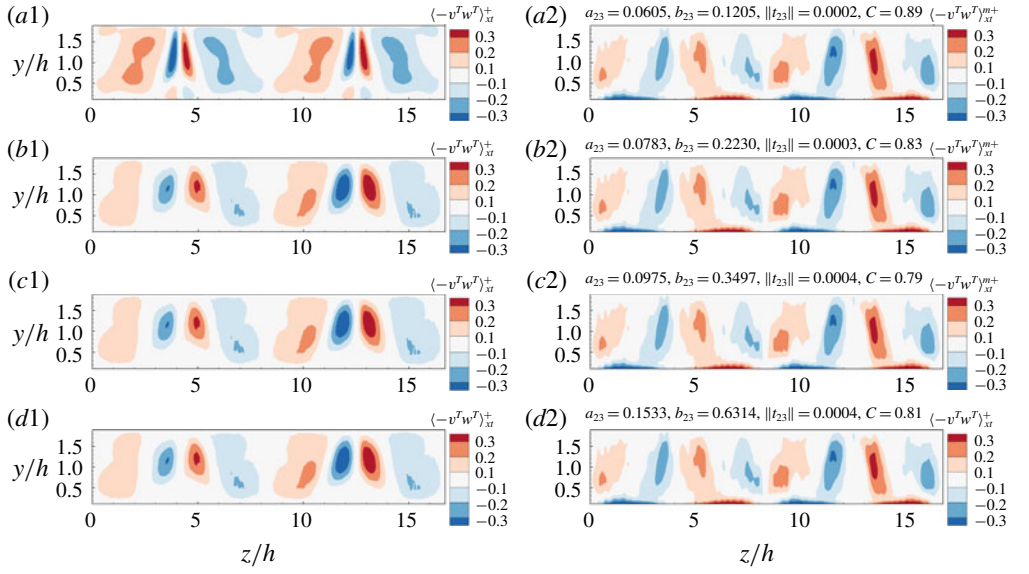

FIGURE 28. Comparison between $\langle -v^T w^T \rangle^+_{xt}$ with the modelled one $\langle -v^T w^T \rangle^{m+}_{xt}$ in the central region ($0.1 < y/h < 1.9$): (*a*1,*b*1,*c*1,*d*1) $\langle -v^T w^T \rangle^+_{xt}$ obtained from the LES and (*a*2,*b*2,*c*2,*d*2) $\langle -v^T w^T \rangle^{m+}_{xt}$ estimated using (5.14); (*a*1,*a*2) $Re_\tau = 1000$, $kh = 0.5$ and $La_t = 0.7$; (*b*1,*b*2) $Re_\tau = 700$, $kh = 0.5$ and $La_t = 0.7$; (*c*1,*c*2) $Re_\tau = 1000$, $kh = 1.0$ and $La_t = 0.7$; and (*d*1,*d*2) $Re_\tau = 1000$, $kh = 0.5$ and $La_t = 0.9$.

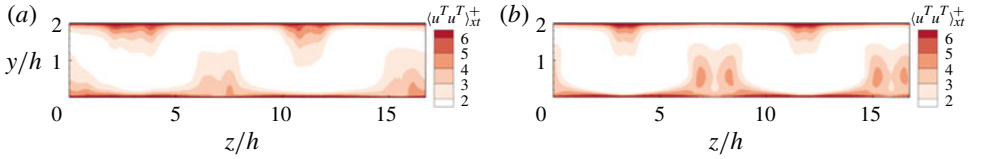

FIGURE 29. Contours of $\langle u^T u^T \rangle^+_{xt}$ at (*a*) $Re_\tau = 10^4$ (case 8) and (*b*) $Re_\tau = 395$ (case 3).

6. Discussion: localizing effect at practical Reynolds number

In the field, the Reynolds number is at least one order of magnitude larger than that in case 1. For the application of the model in § 5 under realistic conditions, it is necessary to verify that the localizing effect of LCs on background turbulence exists at $Re_\tau = O(10^4)$. For this purpose, the localized Reynolds stress $\langle u^T u^T \rangle_{xt}$ is used as an example to study the Reynolds-number effects. Figure 29 compares the contours of $\langle u^T u^T \rangle_{xt}$ of case 8 at $Re_\tau = 10^4$ with those of case 3 at $Re_\tau = 395$. By contrasting figure 29(*a*) to figures 29(*b*) and 5(*a*), it is evident that the distribution of the localized Reynolds stress $\langle u^T u^T \rangle_{xt}$ at $Re_\tau = 10^4$ is similar to that at $Re_\tau = 395$ and $Re_\tau = 1000$ (figure 5*a*). This confirms that the localizing effects of LCs on background turbulence also occurs at a practical Reynolds number.

Additionally, as shown in figure 29, the magnitudes of the localized Reynolds stresses at different Reynolds numbers are comparable. As analysed in § 5, the localized Reynolds stresses $\langle -u_i^T u_j^T \rangle_{xt}$ can be decomposed into $d_{ij} + \langle -u_i^T u_j^T \rangle$, where d_{ij} is related to the LCs and $\langle -u_i^T u_j^T \rangle$ is the background turbulence Reynolds stress averaged over time and horizontal plane. It is noted by Deng *et al.* (2019) that the

intensities of LCs vary slightly with the Reynolds number, and the magnitudes of the Reynolds stresses in the central region of the water column are insensitive to the Reynolds number. Tejada-Martínez & Grosch (2007) also reported that the LCs and the Reynolds stresses in the central region of the water column at $Re_\tau = 180$ are similar to those at $Re_\tau = 395$. The Reynolds number in the wall-resolved LES by Tejada-Martínez & Grosch (2007) and Deng *et al.* (2019) ranges from 180 to 1000, so that the similarity of the turbulence statistics in the central region of the water column found by Tejada-Martínez & Grosch (2007) and Deng *et al.* (2019) indicates the insignificant influence of the Reynolds number. Furthermore, the turbulence statistics in the central region of the water column obtained in the wall-resolved LES of Tejada-Martínez & Grosch (2007) also show agreement with those in the field experiment of Gargett & Wells (2007). It is reasonable to conclude that the magnitudes of the localized Reynolds stresses in the central region of the water column do not show significant Reynolds-number dependence.

7. Conclusions

In shallow-water Langmuir turbulence, the full-depth Langmuir circulations occur in a pattern of counter-rotating vortex pairs, accompanied by positive and negative streamwise velocity fluctuations in the regions dominated by downwelling and upwelling motions of LCs, respectively. In the present study, the database of the wall-resolved LES (Deng *et al.* 2019) and wall-modelled LES of shallow-water Langmuir turbulence based on the Craik–Leibovich equations are analysed to study the localizing effects of large-scale LCs on the small-scale background turbulence. The total velocity is decomposed into a mean part $\langle u_i \rangle$, an LC content part u_i^L and a background turbulence part u_i^T. The streamwise averaging of the total velocity fluctuations u_i' is used to extract the LC content velocity, which is defined as $u_i^L = \langle u_i' \rangle_x$. Because the spanwise location of the LCs remains unchanged with time, a time- and streamwise-averaging approach is adopted to define the localized Reynolds stress as $\langle u_i^T u_j^T \rangle_{xt}$. Based on the LC content velocity, the spanwise domain is divided into three types of regions, namely the U-region, H-region and D-region, where the upwelling, horizontal (spanwise) and downwelling motions are dominant, respectively. The comparison of $\langle u_i^T u_j^T \rangle_{xt}$ in different spanwise regions shows the localizing effects of the LCs on the intensity of background turbulence quantitatively. Through the analyses of the localized Reynolds stresses $\langle u_i^T u_j^T \rangle_{xt}$, it is discovered that the localizing effects of LCs on the background turbulence are different among the near-bottom region, the central region of the water column and the near-surface region. The dominant source terms in the transport equations of the localized Reynolds stresses are then studied to explain the underlying mechanisms of the localization of the background turbulence.

Near the bottom, the localizing effect of LCs on the magnitude of $\langle u^T u^T \rangle_{xt}$ is attributed to the LC content energy production and the mean-shear production. The LC content energy production is correlated to the vertical gradient of u^L. In the D-region and U-region, the value of $\partial u^L / \partial y$ is positive and negative, respectively, consistent with the phase-locked bottom shear stress found by Shrestha & Anderson (2019). As a result, the LC content energy production acts as an additional energy source and sink of $\langle u^T u^T \rangle_{xt}$, respectively. Moreover, the mean-shear production is enhanced and suppressed in the D-region and U-region, respectively. As a result, the magnitude of $\langle u^T u^T \rangle_{xt}$ is larger in the D-region than in the H-region, and is smaller in the U-region than in the H-region. The localization of the magnitudes of $\langle v^T v^T \rangle_{xt}$ and $\langle w^T w^T \rangle_{xt}$ is related to the pressure–strain correlation term, which redistributes the

energy among $\langle u^T u^T\rangle_{xt}$, $\langle v^T v^T\rangle_{xt}$ and $\langle w^T w^T\rangle_{xt}$. Because of the suppression of $\langle u^T u^T\rangle_{xt}$ near the bottom of the U-region, less energy is transferred from $\langle u^T u^T\rangle_{xt}$ to $\langle v^T v^T\rangle_{xt}$ and $\langle w^T w^T\rangle_{xt}$ by the pressure–strain correlation, which leads to the suppression of $\langle v^T v^T\rangle_{xt}$ and $\langle w^T w^T\rangle_{xt}$ in the U-region. In the D-region, the energy of $\langle u^T u^T\rangle_{xt}$ is mainly transferred to $\langle w^T w^T\rangle_{xt}$ by the pressure–strain correlation term. Because of the enhancement of $\langle u^T u^T\rangle_{xt}$ near the bottom of the D-region, more energy is transferred to $\langle w^T w^T\rangle_{xt}$ in the D-region, leading to the enhancement of $\langle w^T w^T\rangle_{xt}$ there. Regarding $\langle v^T v^T\rangle_{xt}$ in the buffer layer of the D-region, it obtains energy mainly from the LC content production with its magnitude smaller than that obtained from the pressure–strain correlation in the H-region, so that the magnitude of $\langle v^T v^T\rangle_{xt}$ is the largest in the H-region.

Near the surface, the dominant source term of $\langle u^T u^T\rangle_{xt}$ is the mean-shear production, which is enhanced and suppressed in the D-region and U-region, respectively. Consequently, the magnitude of $\langle u^T u^T\rangle_{xt}$ is larger in the D-region than in the H-region, and is smaller in the U-region than in the H-region. In the D-region, the dominant source term of $\langle v^T v^T\rangle_{xt}$ is the pressure–strain correlation term, which draws energy from $\langle u^T u^T\rangle_{xt}$. The magnitude of the pressure–strain correlation term is significantly larger in the D-region than in the other two regions, leading to a larger magnitude of $\langle v^T v^T\rangle_{xt}$ in the D-region. The primary energy source of $\langle w^T w^T\rangle_{xt}$ near the surface of the H-region and U-region is the pressure–strain correlation term, while near the surface of the D-region the LC content production acts as an additional source term of $\langle w^T w^T\rangle_{xt}$, leading to the larger magnitude of $\langle w^T w^T\rangle_{xt}$ in the D-region than in the H- and U-regions.

In the central region of the water column, the large-magnitude contours of the five components of the localized Reynolds stress (except for $\langle -v^T w^T\rangle_{xt}$) mainly occur in the lower half of the U-region and the upper half of the D-region. In the lower half of the U-region, the LC content production terms are the key mechanism that leads to the strong localized Reynolds stresses. They act as the dominant sources of $\langle u^T u^T\rangle_{xt}$, $\langle w^T w^T\rangle_{xt}$, $\langle -u^T v^T\rangle_{xt}$ and $\langle -u^T w^T\rangle_{xt}$. Moreover, $\langle v^T v^T\rangle_{xt}$ gains energy from $\langle u^T u^T\rangle_{xt}$ through the redistribution effect of the pressure–strain correlation terms. The large-magnitude LC content production terms are also responsible for the enhancement of $\langle u^T u^T\rangle_{xt}$, $\langle w^T w^T\rangle_{xt}$ and $\langle -u^T w^T\rangle_{xt}$ in the upper half of the D-region. Similar to the lower half of the U-region, the energy held by $\langle u^T u^T\rangle_{xt}$ is also redistributed to $\langle v^T v^T\rangle_{xt}$ to induce a large magnitude of $\langle v^T v^T\rangle_{xt}$ there. However, different from the lower half of the U-region, the Stokes forcing term works as the dominant source of the enhanced $\langle -u^T v^T\rangle_{xt}$ in the upper half of the D-region. The large-magnitude $\langle -v^T w^T\rangle_{xt}$ appears in the vertically central area of the D-region, due to the contribution of the LC content production.

Based on the analyses of the dominant sources in the transport equations of the localized Reynolds stresses, predictive models are proposed to scale the localized Reynolds normal stress $\langle u^T u^T\rangle_{xt}$ in the near-bottom region and the localized Reynolds shear stresses $\langle -u^T v^T\rangle_{xt}$, $\langle -u^T w^T\rangle_{xt}$ and $\langle -v^T w^T\rangle_{xt}$ in the central region of the water column. A new characteristic velocity scale u^l based on the local wall shear stress is used to normalize $\langle u^T u^T\rangle_{xt}$ and vertical coordinate. This new scaling for the profiles of $\langle u^T u^T\rangle_{xt}$ works well in the near-bottom region in various cases with different values of the Reynolds number, turbulent Langmuir number and wavenumber. The models of $\langle -u^T v^T\rangle_{xt}$, $\langle -u^T w^T\rangle_{xt}$ and $\langle -v^T w^T\rangle_{xt}$ are proposed based on the dominant mechanism underlying the localizing effects. The vertical and spanwise variations of u^L together with the vertical gradient of the Stokes drift velocity are used to predict $\langle -u^T v^T\rangle_{xt}$. The value of $\langle -u^T w^T\rangle_{xt}$ is found to be approximately proportional

to $\partial u^L/\partial z$. The magnitude of $\langle -v^T w^T \rangle_{xt}$ is found to be approximately determined by the linear combination of $\partial v^L/\partial z$ and $\partial w^L/\partial y$. The contour patterns of the localized Reynolds shear stresses obtained from the proposed model are in agreement with the LES results. These models show the spatial dependence of Boussinesq-model parameters. These models can be extended to practical Reynolds numbers, because similar localizing effects are observed in the wall-modelled LES of shallow-water Langmuir turbulence at $Re_\tau = O(10^4)$.

The localization effects described in this work show the significant nonlinear interaction between LCs and background turbulence in shallow-water Langmuir turbulence. The mechanisms underlying the localization effects revealed in this study provide physical insights into how the large-scale motions influence smaller-scale turbulence, which has been an active research topic in the wall-bounded turbulent flows. The results of this study deepen the fundamental understanding of the flow physics associated with LCs in shallow water, and establish a physical foundation for the development of turbulence models for this type of flow. The models proposed in this study are a first step towards the physical-based modelling of such flows and can be used to predict the localized intensities of background turbulence based on the information of the LC content velocity field.

Acknowledgements

The authors gratefully acknowledge the anonymous referees for their constructive and valuable comments. This work is partially supported by Office of Naval Research, National Science Foundation, and Minnesota Sea Grant.

Declaration of interests

The authors report no conflict of interest.

Supplementary material

Supplementary material is available at https://doi.org/10.1017/jfm.2020.215.

Appendix. Effects of the computational domain size on the localized Reynolds stresses

As reported by Gloshan *et al.* (2017), the large-scale streaks observed from the instantaneous velocity field of u' in shallow-water Langmuir turbulence meanders in a large computational domain size. To examine the influence of the computational domain size and the meandering of large-scale streaks on our analysis, we conducted case 7 using a much larger computational domain size $32\pi h \times 2h \times 64\pi h/3$ (see table 1). The other parameters of case 7 remain the same as those of case 3. Figure 30(*a*) shows the instantaneous velocity field of u' at $y/h = 0.038$ for case 7. Similar to the finding of Gloshan *et al.* (2017), the large-scale streaks of u' slightly meander along the streamwise direction. Figure 30(*b*,*c*) compares the contours of $\langle u^T u^T \rangle_{xt}$ in cases 3 and 7. It can be seen that the localized distribution of $\langle u^T u^T \rangle_{xt}$ obtained from the large computational domain size agrees with that obtained from the small computational domain size. Specifically, the large magnitude of $\langle u^T u^T \rangle_{xt}$ is located in the lower half of the U-region and the upper half of the D-region. Therefore, the computational domain size used in cases 1–6 (table 1) is sufficient for the convergence of the results, and the slight meandering of the large-scale streaks has little impact on the results presented in this study.

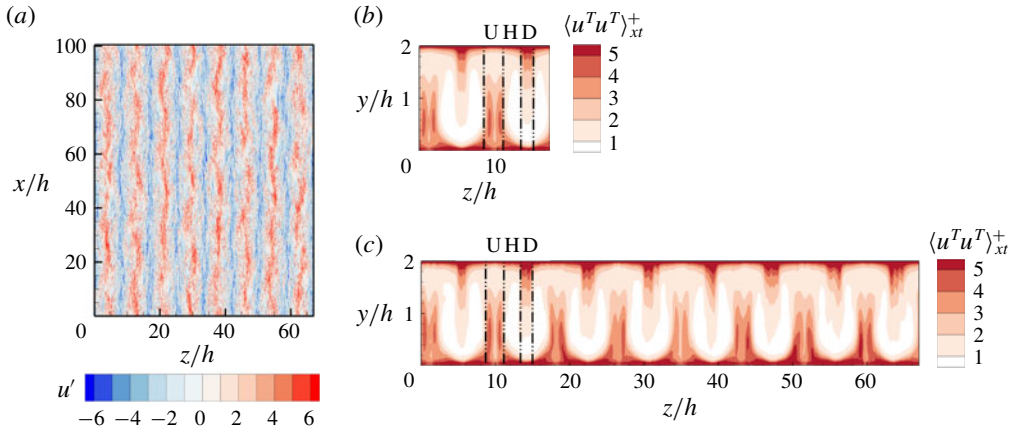

FIGURE 30. (*a*) Instantaneous fields of u' on the x–z plane in case 7, and the contours of $\langle u^T u^T \rangle_{xt}$ in (*b*) case 3 and (*c*) case 7.

REFERENCES

AKAN, C., TEJADA-MARTÍNEZ, A. E., GROSCH, C. E. & MARTINAT, G. 2013 Scalar transport in large-eddy simulation of Langmuir turbulence in shallow water. *Cont. Shelf Res.* **55**, 1–16.

ANDERSON, W. 2016 Amplitude modulation of streamwise velocity fluctuations in the roughness sublayer: evidence from large-eddy simulations. *J. Fluid Mech.* **789**, 567–588.

ASSAF, G., GERARD, R. & GORDON, A. L. 1971 Some mechanisms of oceanic mixing revealed in aerial photographs. *J. Geophys. Res.* **76**, 6550–6572.

BALARAS, E., BENOCCI, C. & PIOMELLI, U. 1995 Finite-difference computations of high Reynolds number flows using the dynamic subgrid-scale model. *Theor. Comput. Fluid Dyn.* **7**, 207–216.

BARSTOW, S. F. 1983 The ecology of Langmuir circulation: a review. *Mar. Environ. Res.* **9** (4), 211–236.

BELCHER, S. E., GRANT, A. L., HANLEY, K. E., FOX-KEMPER, B., VAN-ROEKEL, L., SULLIVAN, P. P., LARGE, W. G., BROWN, A., HINES, A., CALVERT, D. *et al.* 2011 A global perspective on Langmuir turbulence in the ocean surface boundary layer. *Geophys. Res. Lett.* **39** (18), L18605.

BERNARDINI, M., PIROZZOLI, S. & ORLANDI, P. 2014 Velocity statistics in turbulent channel flow up to $Re_\tau = 4000$. *J. Fluid Mech.* **742**, 171–191.

CHAPMAN, D. R. 1979 Computational aerodynamics development and outlook. *AIAA J.* **17**, 1293–1313.

CHOI, H. & MOIN, P. 2012 Grid-point requirements for large eddy simulation: Chapman's estimates revisited. *Phys. Fluids* **24**, 011702.

CRAIK, A. D. D. & LEIBOVICH, S. 1976 A rational model for Langmuir circulations. *J. Fluid Mech.* **73**, 401–426.

DAI, Y. J., HUANG, W. X. & XU, C. X. 2016 Effects of Taylor–Görtler vortices on turbulent flows in a spanwise-rotating channel. *Phys. Fluids* **28** (11), 115104.

D'ASARO, E. A. 2014 Turbulence in the upper-ocean mixed layer. *Annu. Rev. Mar. Sci.* **6**, 101–115.

DENG, B. Q., HUANG, W. X. & XU, C. X. 2016 Origin of effectiveness degradation in active drag reduction control of turbulent channel flow at $Re_\tau = 1000$. *J. Turbul.* **17**, 758–786.

DENG, B. Q., YANG, Z., XUAN, A. & SHEN, L. 2019 Influence of Langmuir circulations on turbulence in the bottom boundary layer of shallow water. *J. Fluid Mech.* **861**, 275–308.

DETHLEFF, D. & KEMPEMA, E. W. 2007 Langmuir circulation driving sediment entrainment into newly formed ice: tank experiment results with application to nature (Lake Hattie, United States; Kara Sea, Siberia). *J. Geophys. Res.* **112**, C02004.

DIERSSEN, H. M., ZIMMERMAN, R. C., DRAKE, L. A. & BURDIGE, D. J. 2009 Potential export of unattached benthic macroalgae to the deep sea through wind-driven Langmuir circulation. *Geophys. Res. Lett.* **36**, L04602.

FARMER, D. & LI, M. 1995 Patterns of bubble clouds organized by Langmuir circulation. *J. Phys. Oceanogr.* **25**, 1426–1440.

GARGETT, A., WELLS, J., TEJADA-MARTÍNEZ, A. E. & GROSCH, C. E. 2004 Langmuir supercells: a mechanism for sediment resuspension and transport in shallow seas. *Science* **306**, 1925–1928.

GARGETT, A. E. & GROSCH, C. E. 2014 Turbulence process domination under the combined forcings of wind stress, the Langmuir vortex force, and surface cooling. *J. Phys. Oceanogr.* **44** (1), 44–67.

GARGETT, A. E., SAVIDGE, D. K. & WELLS, J. R. 2014 Anatomy of a Langmuir supercell event. *J. Mar. Res.* **72** (3), 127–163.

GARGETT, A. E. & WELLS, J. R. 2007 Langmuir turbulence in shallow water. Part 1. Observations. *J. Fluid Mech.* **576**, 27–61.

GEMMRICH, J. R. & FARMER, D. M. 1999 Near-surface turbulence and thermal structure in a wind-driven sea. *J. Phys. Oceanogr.* **29** (3), 480–499.

GERBI, G. P., TROWBRIDGE, J. H., TERRAY, E. A., PLUEDDEMANN, A. J. & KUKULKA, T. 2009 Observations of turbulence in the ocean surface boundary layer: energetics and transport. *J. Phys. Oceanogr.* **39** (5), 1077–1096.

GERMANO, M., PIOMELLI, U., MOIN, P. & CABOT, W. H. 1991 A dynamic subgrid-scale eddy viscosity model. *Phys. Fluids* A **3**, 1760–1765.

GLOSHAN, R., TEJADA-MARTÍNEZ, A. E., JUHA, M. J. & BAZILEVS, Y. 2017 LES and RANS simulation of wind- and wave-forced oceanic turbulent boundary layers in shallow water with wall modeling. *Comput. Fluids* **142**, 96–108.

GROSCH, C. E. & GARGETT, A. E. 2016 Why do LES of Langmuir supercells not include rotation? *J. Phys. Oceanogr.* **46** (12), 3595–3597.

HARCOURT, R. R. 2013 A second-moment closure model of Langmuir turbulence. *J. Phys. Oceanogr.* **43**, 675–697.

HOWLAND, M. F. & YANG, X. I. A. 2018 Dependence of small-scale energetics on large scales in turbulent flows. *J. Fluid Mech.* **852**, 641–662.

HOYAS, S. & JIMÉNEZ, J. 2008 Reynolds number effects on the Reynolds-stress budgets in turbulent channels. *Phys. Fluids* **20**, 101511.

HUTCHINS, N. & MARUSIC, I. 2007 Large-scale influences in near-wall turbulence. *Proc. R. Soc. Lond.* A **365**, 647–664.

INOUE, M., MATHIS, R., MARUSIC, I. & PULLIN, D. I. 2012 Inner-layer intensities for the flat-plate turbulent boundary layer combining a predictive wall-model with large-eddy simulations. *Phys. Fluids* **24**, 075102.

JIMENEZ, J. 2012 Cascades in wall-bounded turbulence. *Annu. Rev. Fluid Mech.* **44**, 27–45.

KIM, J. & MOIN, P. 1985 Application of a fractional-step method to incompressible Navier–Stokes equations. *J. Comput. Phys.* **59**, 308–323.

KUKULKA, T. & HARCOURT, R. R. 2017 Influence of Stokes drift decay scale on Langmuir turbulence. *J. Phys. Oceanogr.* **47** (7), 1637–1656.

KUKULKA, T., PLUEDDEMANN, A. J. & SULLIVAN, P. P. 2012 Nonlocal transport due to Langmuir circulation in a coastal ocean. *J. Geophys. Res.* **117**, C12007.

KUKULKA, T., PLUEDDEMANN, A. J., TROWBRIDGE, J. H. & SULLIVAN, P. P. 2011 The influence of crosswind tidal currents on Langmuir circulation in a shallow ocean. *J. Geophys. Res.* **116**, C08005.

LANGMUIR, I. 1938 Surface motion of water induced by wind. *Science* **87**, 119–123.

LEIBOVICH, S. 1977 On the evolution of the system of wind drift currents and Langmuir circulations in the ocean. *J. Fluid Mech.* **79**, 715–743.

LEIBOVICH, S. 1983 The form and dynamics of Langmuir circulations. *Annu. Rev. Fluid Mech.* **15**, 391–427.

LI, S., LI, M., GERBI, G. P. & SONG, J. B. 2013 Roles of breaking waves and Langmuir circulation in the surface boundary layer of a coastal ocean. *J. Geophys. Res.* **118** (10), 5173–5187.

LILLY, D. K. 1992 A proposed modification of the Germano subgrid-scale closure method. *Phys. Fluids* **4**, 633–635.

MARTINAT, G., GROSCH, C. E. & GATSKI, T. B. 2014 Modeling of Langmuir circulation: triple decomposition of the Craik–Leibovich model. *Flow Turbul. Combust.* **92** (1–2), 395–411.

MARTINAT, G., XU, Y., GROSCH, C. E. & TEJADA-MARTÍNEZ, A. E. 2011 LES of turbulent surface shear stress and pressure-gradient-driven flow on shallow continental shelves. *Ocean Dyn.* **61** (9), 1369–1390.

MATHIS, R., HUTCHINS, N. & MARUSIC, I. 2009 Large-scale amplitude modulation of the small-scale structures in turbulent boundary layers. *J. Fluid Mech.* **628**, 311–337.

MCWILLIAMS, J. C., SULLIVAN, P. P. & MOENG, C. H. 1997 Langmuir turbulence in the ocean. *J. Fluid Mech.* **334**, 1–30.

PAPAVASSILIOU, D. V. & HANRATTY, T. J. 1997 Interpretation of large-scale structures observed in a turbulent plane Couette flow. *Intl J. Heat Fluid Flow* **18**, 55–69.

PIOMELLI, U. & BALARAS, E. 2002 Wall-layer models for large-eddy simulations. *Annu. Rev. Fluid Mech.* **34**, 349–374.

POPE, S. B. 2001 *Turbulent Flows*. Cambridge University Press.

REYNOLDS, W. C. & HUSSAIN, A. K. 1972 The mechanics of an organized wave in turbulent shear flow. Part 3. Theoretical models and comparisons with experiments. *J. Fluid Mech.* **54** (2), 263–288.

SALESKY, S. T. & ANDERSON, W. 2018 Buoyancy effects on large-scale motions in convective atmospheric boundary layers: implications for modulation of near-wall processes. *J. Fluid Mech.* **856**, 133–168.

SAVIDGE, D. K. & GARGETT, A. E. 2017 Langmuir supercells on the middle shelf of the South Atlantic Bight: 1. Cell structure. *J. Mar. Res.* **75** (2), 49–79.

SCOTT, J. T., MYER, G. E., STEWART, R. & WALTHER, E. G. 1969 On the mechanism of Langmuir circulations and their role in epilimnion mixing. *Limnol. Oceanogr.* **14**, 493–503.

SHRESTHA, K. & ANDERSON, W. 2019 Coastal Langmuir circulations induced phase-locked modulation of bathymetric stress. *Environ. Fluid Mech.,* 1–12.

SHRESTHA, K., ANDERSON, W. & KUEHL, J. 2018 Langmuir turbulence in coastal zones: structure and length scales. *J. Phys. Oceanogr.* **48**, 1089–1115.

SHRESTHA, K., TEJADA-MARTINEZ, A. & KUEHL, J. 2019 Orientation of coastal-zone Langmuir cells forced by wind, wave and mean current at variable obliquity. *J. Fluid Mech.* **879**, 716–743.

SINHA, N., TEJADA-MARTÍNEZ, A. E., AKAN, C. & GROSCH, C. E. 2015 Toward a K-profile parameterization of Langmuir turbulence in shallow coastal shelves. *J. Phys. Oceanogr.* **45** (12), 2869–2895.

SKYLLINGSTAD, E. D. & DENBO, D. W. 1995 An ocean large eddy simulation of Langmuir circulations and convection in the surface mixed layer. *J. Geophys. Res.* **100**, 8501–8522.

SMARGORINSKY, J. 1963 General circulation experiments with the primitive equations: I. The basic experiment. *Mon. Weath. Rev.* **91**, 99–164.

SMITH, A. J., MCKEON, B. J. & MARUSIC, I. 2011 High-Reynolds number wall turbulence. *Annu. Rev. Fluid Mech.* **43**, 353–375.

SMITH, J. A. 1992 Observed growth of Langmuir circulation. *J. Geophys. Res.* **97**, 5651–5664.

SMITH, J. A. 2001 *Fluid Mechanics and the Environment: Dynamical Approaches*. Springer.

SULLIVAN, P. P. & MCWILLIAMS, J. C. 2010 Dynamics of winds and currents coupled to surface waves. *Annu. Rev. Fluid Mech.* **42**, 19–42.

TAKAGAKI, N., KUROSE, R., TSUJIMOTO, Y., KOMORI, S. & TAKAHASHI, K. 2015 Effects of turbulent eddies and Langmuir circulations on scalar transfer in a sheared wind-driven liquid flow. *Phys. Fluids* **27**, 016603.

TEJADA-MARTÍNEZ, A. E., AKAN, C., SINHA, N., GROSCH, C. E. & MARTINAT, G. 2013 Surface dynamics in LES of full-depth Langmuir circulation in shallow water. *Phys. Scr.* **2013**, 014008.

TEJADA-MARTÍNEZ, A. E. & GROSCH, C. E. 2007 Langmuir turbulence in shallow water. Part 2. Large-eddy simulation. *J. Fluid Mech.* **576**, 63–108.

TEJADA-MARTÍNEZ, A. E., GROSCH, C. E., SINHA, N., AKAN, C. & MARTINAT, G. 2012 Disruption of the bottom log layer in large-eddy simulations of full-depth Langmuir circulation. *J. Fluid Mech.* **699**, 79–93.

THORPE, S. A. 1992 The breakup of Langmuir circulation and the instability of an array of vortices. *J. Phys. Oceanogr.* **22**, 350–360.

THORPE, S. A. 2004 Langmuir circulation. *Annu. Rev. Fluid Mech.* **36**, 55–79.

WALKER, R., TEJADA-MARTÍNEZ, A. E. & GROSCH, C. E. 2016 Large-eddy simulation of a coastal ocean under the combined effects of surface heat fluxes and full-depth Langmuir circulation. *J. Phys. Oceanogr.* **46** (8), 2411–2436.

WELLER, R. A. & PRICE, J. F. 1988 Langmuir circulation within the oceanic mixed layer. *Deep Sea Res.* A **35**, 711–747.

YIN, G., HUANG, W. X. & XU, C. X. 2018 Prediction of near-wall turbulence using minimal flow unit. *J. Fluid Mech.* **841**, 654–673.